Masters Theses & Specialist Projects   Graduate School

Summer 2017

Synthesis,Structure and Properties of Ruthenium Polypyridyl Metalloligand Based Metal-Organic Frameworks

Mamatha Polapally
Western Kentucky University, mamatareddy.a@gmail.com

Follow this and additional works at: http://digitalcommons.wku.edu/theses

Part of the Materials Chemistry Commons, Polymer and Organic Materials Commons, and the Structural Materials Commons

SYNTHESIS, STRUCTURE, AND PROPERTIES OF RUTHENIUM POLYPYRIDYL
METALLOLIGAND BASED METAL-ORGANIC FRAMEWORKS

A Thesis
Presented to
The Faculty of the Department of Chemistry
Western Kentucky University
Bowling Green, Kentucky

In Partial Fulfillment
Of the Requirements for the Degree
Master of Science

By
Mamatha Polapally

August 2017

SYNTHESIS, STRUCTURE, AND PROPERTIES OF RUTHENIUM POLYPYRIDYL METALLOLIGAND BASED METAL-ORGANIC FRAMEWORKS

Date Recommended __7- 14 -17__

Bangbo Yan

Dr. Bangbo Yan, Director of Thesis

Er Conte

Dr. Eric Conte

S Gupta

Dr. Sanju Gupta

T. Scott __7/31/17__

Dean, Graduate Studies and Research   Date

I dedicate this thesis to my parents (Narsimha Reddy Anugandula & Manjula Anugandula), my husband (Srikanth Reddy) and especially to my lovely daughter (Samanvi Reddy) for their endless support, unconditional love and to my research advisor Dr. Bangbo Yan who supported and encouraged me throughout the journey of this project at Western Kentucky University

ACKNOWLEDGEMENTS

husband, in-laws and to all my family members for their support and my deepest love to my daughter, who blessed me with a life of joy. I am so proud of her.

TABLE OF CONTENTS

LIST OF FIGURES

LIST OF TABLES

SYNTHESIS, STRUCTURE, AND PROPERTIES OF RUTHENIUM POLYPYRIDYL METALLOLIGAND BASED METAL-ORGANIC FRAMEWORKS

Mamatha Polapally   August 2017   Pages 77

Directed by: Dr. Bangbo Yan, Dr. Eric Conte, Dr. Sanju Gupta

Department of Chemistry   Western Kentucky University

Metal-organic frameworks (MOFs) have been extensively studied because of their amazing applications in gas storage, purification, photocatalysis, chemical sensing, and imaging techniques. Ruthenium polypyridyl complexes have been broadly considered as photosensitizers for the conversion of solar energy and photoelectronic materials. With this aspect, we have synthesized three new ruthenium polypyridyl based MOFs ($[Ru(H_2bpc)Cu(bpc)(Hbpc)_2(H_2O)]\cdot 5H_2O$ (**1**), $[Ru(H_2bpc)(Fe(bpc)(Hbpc)_2(H_2O)_2]\cdot 6H_2O$ (**2**) and $[Ru(H_2bpc)Ni(bpc)(Hbpc)_2(H_2O)_2]\cdot 6H_2O$ (**3**)) from ruthenium(III) chloride, bpc (2,2'- bipyridine-4,4'-dicarboxylic acid) ligand, and $3d$ M(II) metal ions (M(II)= Cu(II), Fe(II), Ni(II)). These MOFs were synthesized under hydro or solvothermal conditions by using water, ethanol or methanol as solvents. The crystal structures of the new compounds contains zigzag chains of $[Ru(bpc)_3]^{n-}$ complex ions linked by Cu, Fe or Ni complex ions individually. Above synthesized crystal structures were characterizing by single-crystal X-ray and powder X-ray diffraction strategies, UV-vis and IR spectroscopy. Thermal properties were determining by thermogravimetric analysis. Magnetic properties were also studied.

CHAPTER 1

INTRODUCTION

In the today's world, almost 80% of the energy supply is depend on fossil fuels and mankind is facing a serious problem because of the fast consumption of fossil fuels and increasing levels of carbon dioxide (CO_2) and other harmful chemicals in the atmosphere. The current global energy depletion rate of 16.3TW (2012) will be around 40TW by 2050, and 60TW by 2100.[1] According to the Intergoveral Panel on Climate Change (IPCC) predictions, CO_2 levels may rise up to 590ppm by the year 2100 when the global temperature may increase by 1.9°C.[2] As per the assessment report (2014) of IPCC, the greenhouse gases (GHGs) level is increasing drastically. The slow increase rate of +1.3% per year (1970-2000) has changed drastically to +2.2% per year (2000 onward),[3] especially, the CO_2 level in the atmosphere, which leads to global climate changes.

1.1 Role of Carbon Dioxide Gas in Climate Change

CO_2 is one of the major pollutant and an essential greenhouse gas in the atmosphere. The CO_2 level in the atmosphere is 400 ppm and has been steadily increasing since the beginning of the modern transformation in the late 18th century.[4] Antarctic ice center data indicate that for the 420,000 years preceding to this fast increase CO_2 levels in the atmosphere, the amount of CO_2 in the environment wavered bit by bit over the scope of 150 ppm to 300 ppm.[5] It is clear from this information that worldwide industrialization has prompt in climatic CO_2 concentrations at a higher rate than naturally expected. It is emitted into the atmosphere by various human-related activities such as combustion of fossil fuels (coal, oil, natural gas), transportation, agricultural waste, household waste etc.[6] More CO_2 emissions in the atmosphere can increase the greenhouse effect where by CO_2 gases trap

thermal radiation near the earth's surface. With increasing CO_2 levels in the atmosphere, the global temperature raised to $0.76^\circ C$ since 1907. [7] The continuous increasing rate of CO_2 emission on its current path will result in drastic change in the global climate, and lead to sea level rise, harm to delicate territories and an irreversible increase of ocean acidity levels with an unwanted effect on the environment and other critical consequences.[8]

Using alternative fuels or converting CO_2 to the useful fuel forms would help to balance the CO_2 levels in the atmosphere. Elimination or reduction of CO_2 emissions is a conceivable approach to avoid irrevocable damage to the global atmosphere. For the benefits of nature and human beings, actions must be undertaken to reduce the CO_2 levels in the atmosphere. We can promote low carbon or carbon- free energy sources such as solar, the wind and nuclear power sources.[9] One of the important approach for the clean environment is the generation of useful or valuable fuels by using solar energy. With this aspect, researchers are attempting to develop efficient photocatalysts for water splitting or CO_2 reduction to useful fuels (H_2, CO, $HCOOH$, $HCHO$, CH_4) using solar energy.

1.2 Photocatalytic Reduction of CO_2

Reduction or elimination of carbon dioxide (CO_2) in the atmosphere is one of the best solutions to solve the global climatic changes. It is not only a greenhouse gas but also a renewable carbon feedstock for the production of high energy or valuable chemicals. In nature, plants and other microorganisms utilize CO_2 to store solar energy via natural photosynthesis process. In plants and microorganisms, this process convert atmospheric CO_2 and H_2O to oxygen and carbohydrates in presence of sunlight (solar energy).[10]

$$6CO_2 + 6\ H_2O \rightarrow\ C_6H_{12}O_6 + 6O_2$$
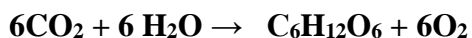
The photosynthetic reaction can be divided into two half reactions, which are oxidation and reduction. In the above reaction, water molecules are photo oxidized by the absorption of sunlight, and to release oxygen and protons. The second phase of this reaction is a light independent reaction that converts CO_2 into glucose and oxygen. Nowadays, researchers are trying to develop new chemical process that replicates the natural photosynthesis, and ways of transforming unwanted CO_2 into useful or valuable chemicals such as CO, HCOOH, CH_4 etc. These new methods are called artificial photosynthetic methods of CO_2 reduction.[11]

In the artificial photosynthetic process, the compound that absorbs solar light is called photosensitizer. One of the simplest designs in this process is that the photosensitizer is linked to the catalyst. The process involves two reactions.

1) The photosensitizer transfer electrons to the catalyst when it absorbs solar light, becoming oxidized in the process.

2) This drives the catalyst which reduces CO_2 into valuable or useful gases such as HCOOH, CO, CH_4 etc.[12]

The schematic diagram of photocatalytic reduction of CO_2 is shown below:

D (electron donor) → P(photosensitizer) →C(catalyst) →CO$_2$ →useful products
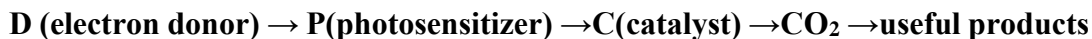
Carbon dioxide reduction can be carried out in both liquid and gaseous phases. In the liquid phase, the limited solubility of CO_2 in water is a critical issue to drive efficient photocatalytic CO_2 reduction. The solubility of CO_2 in water can be enhanced by utilizing additives such as NaOH, $NaHCO_3$, $NaCO_3$.[13] These additives improve CO_2 solubility via bicarbonate reduction. The resulting carbonate species are more difficult to get absorbed

3

on the catalyst surface and have different reduction potentials. In this case, surface absorption of water is more preferable than CO_2 in the liquid phase. Thus, the reduction of water is more suitable than the reduction of CO_2. On the other hand, gaseous phase CO_2 reduction reactions can be carried out with humidified CO_2. In order to improve these reactions, Xie et al [14] have introduced TiO_2 and pt-TiO_2 as photocatalysts and studied CO_2 reduction reactions in both liquid and gaseous phase. They found the CH_4 yield is more than H_2 production in gaseous phase when compared to the liquid phase photocatalytic reactions. Later, quantum dots were introduced as photocatalysts due to their large surface area for the absorption of water and shorter charge transfer reactions.[15] These provides more potential energy for photochemical reactions because of quantum confinement.[16] But the efficiency of photocatalysts depends on their morphology, exposed size and surface vacancy. The different chemical species (CO_3, HCO_3 etc) get absorbed on the surface of photocatalysts in a different extent and possess different reduction potentials.[17] Thus addition of NaOH, which favors the dissolution of CO_2 there by increases the efficiency of CO_2 photocatalytic reduction on TiO_2 supported Cu catalysts.[18] But in the gas phase photocatalytic reaction is effected by surface properties of the photocatalysts, temperature, CO_2-H_2O ratio. The presence of organic absorbent molecules (methanol, formic acid, acetic acid) on the surface of the photocatalysts plays a crucial role in the photocatalytic reduction of CO_2. The presence of acetic acid (CH_3COOH) absorbents on the surface of catalysts, can lead to the formation of methanol(CH_4) via Photo-Kolbe reaction.[19] Thus without any organic absorbents, photocatalysis shows a negligible amount of methanol production.[20]

A systematic study of the photochemical as well photoelectrochemical reduction of CO_2 was carried out in aqueous suspensions of semiconductor powders such as TiO_2, ZnO, CdS etc.[21] The yields of methanol are well correlated with the conduction band edge position of semiconductors, which indicates a negative conduction band edge relative to the CO_2 reduction potential. Since the discovery of photocatalysis process for CO_2 reduction on a TiO_2 photocatalyst by Fujishma and Honda,[22] a number of effects are focused on the TiO_2 based catalysis due to their large bandgap (3.2ev) of TiO_2, which limits its photocatalytic activity under visible light irradiation. [23-25]

During the past decade, a lot of efforts have been devoted to modifying TiO_2 via ion doping and deposition of metals on the surface of TiO_2 semiconductor for a better utilization of light.[26-27] Meanwhile, deposition of metals such as Au, Ag, Cu on the surface of TiO_2 photoctalysts improves the photocatalytic activity. For example, Ag deposited TiO_2 semiconducting materials show superior activities for CO_2 reduction due to the binding with CO. Here, Ag efficiently reduces CO_2 into CO from the separate reaction sites such as oxidation and reduction.[28] Coupling of semiconductors with bimetallic systems also shown good results of activity. For example, Cu-Pt bimetallic systems loaded on TiO_2 nanotubes (Cu -Pt/TiO_2) can reduce CO_2 to CH_4, C_2H_4 etc. with 4-fold improvement under solar irradiation and in presence of water.[29] Co-deposition of reduction and oxidation catalysts such as RuO_2 and Pt on Zn_2GeO_4, which causes significant improvement in methanol production. Liu et al. have used $ZnGeN_2O_x$ nano materials for the reduction of CO_2 to CH_4 under visible light irradiation. The resulting products have still negligible amount of methanol and oxygen production.[30]

Huang et al.[31] have developed multicomponent photocatalytic systems, which consist of two components, i.e. a mononuclear C_2H_5-RuH complex oxo-bridged with TiO_2 for photochemical reduction of CO_2 to methanol under visible light irradiation. It showed a maximum photocatalytic activity at a Ru loading of 0.5 wt% on TiO_2. The higher activity of the catalysts for CO_2 reduction is attributed to the long-lived charge separated state. Graphitic C_3N_4 has been used as photocatalyst due to its high stability and visible responsive. Other multicomponent photocatalysts were also investigated by different researchers such as semiconductor homo[32] & hetero[33] structures and Z-scheme TiO_2 based multi component photocatalsts.[34] These multicomponent TiO_2-based photocatalysts have significantly enhanced the efficiency of photochemical reduction of CO_2. In spite of these exciting developments for the photocatalytic reduction of CO_2 in recent years, it remains a great challenge to develop a system that can efficiently use full spectrum length of solar radiation with high efficiency, acceptable stability.

Using the similar strategy for TiO_2-based photocatalysts, ZnO/Cds hetero structures are demonstrated based to be more active photocatalysts for H_2 evolution under solar light irradiation. Unlike semiconductor based photosystems, which are not efficient ways of gathering these molecular functional components into hierarchical organizations to transfer sunlight energy into chemical energy, metal organic frameworks have been introduced as photocatalysts for the photochemical reduction of CO_2.[35]

1.3 Metal-Organic Frameworks as Photocatalysts

Metal organic frameworks (MOFs) have been proposed as potential photocatalysts since the late 1990's and the early 2000's.[36] MOFs are a new class of crystalline solids, consisting of metal ions or clusters (meta-based nodes) coordinated by organic ligands.

They can serve as an ideal platform for the improvement of next generation potential photocatalysts due to their high affinity, their chemical and structural tenability and their broad UV-visible absorption bands. Their absorption band can be allocated to a localized metal-to-ligand charge transfer (MLCT) or ligand-to-metal charge transfer(LMCT) transition or a π- π^* transition of the aromatic ligand. Taking advantage of broad absorption of MLCT or ligand π- π^* bands, many photocatalytic MOFs have been reported. In addition to absorption, charge separation between the metal and ligand is the second advantage of MOFs as photocatalysts. Bridging ligands based organic and metal-organic chromophores have also used as building blocks to construct photocatalytic MOFs.

With the best knowledge about photophysical properties of organic ligands (chromophores) and effective charge transfer abilities, MOF photocatalysts can be designed with high efficiency to promote more advanced, and useful reactions. The more advanced designs utilize more than one functional component in the framework. For instance, metal nanoparticles were integrated as a co-catalyst for diffusion either hydrogen evolution.[37-38] Multicomponent MOFs provide important advantages in performing these photocatalytic reactions as the different components in the MOFs commonly interact to provide enhanced catalytic performances.[39]

1.3.1 Energy Transfer and Light Harvesting in MOFs

Efficient energy (charge) transfer has been observed in between donor-acceptor ligand pairs or between ligand and guest compounds in MOFs.[40-41] In 2009, Loh and coworkers[6] investigated the efficient energy transfer occurred in between conjugated chromophores in a 1-D nanoscale coordination polymer. Hupp and coworkers[42] enclosed CdSe/ZnS core

quantum dots into the MOF channel, and observed charge transfer between quantum dots and porphyrin-derived ligands of the frameworks.

Recently, researchers have utilized the MOFs as light-harvesting complexes and studied charge transfer behaviors over long distances. For example, in 2010, Lin, Meyer and coworkers[43] reported a phosphorescent MOF [Zn(L_1-Ru)]·2DMF·4H_2O, which can be excited to the MLCT state of the L_1-Ru bridging ligand   and show phosphorescence with several hundreds of nanoseconds lifetime. Reddy and coworkers[44] studied the energy transfer between different lanthanide ions such as Tb^+, Eu^{+3} in a mixed lanthanide MOF [$Eu_{0.5}Tb_{0.5}L_3(H_2O)_2$]$_n$ [L= 4-(dipyrin-2-yl) aminobenzoate]. The efficiency of energy transfer reported to be 86% based on lifetime measurements.

1.3.2 MOFs for Photocatalytic H_2 Evolution and CO_2 Reduction

Light driven water splitting or reduction of CO_2 is one of the most important scenarios for solar energy conversion. Due to MLCT and ligand π- π* transition in the UV and visible regions, MOFs exhibit similar photocatalytic activities to semiconductors. For example, UiO-66 [45] has been used as photocatalysts for H_2 evolution and it exhibited catalytic activity in a methanol-H_2O solution. When amino (NH_2) group was introduced into UiO-66, the resulting MOF (NH_2-UiO-66) has a broad absorption band between 300-400 nm and slightly enhanced photocatalytic activity towards CO_2 reduction recently.[46] Using similar strategy, in 2012, Li and coworkers constructed the MOF [NH_2-MIL-125(Ti)] and it exhibits a visible absorption band extending to 550nm. The MOF has been showed photocatalytic activity for CO_2 reduction with TON (0.03) per Ti under visible light performance. The photocatalytic activities of these simple MOFs are very low (TON is less than 1), although photo-mediated reactions can be achieved. This low activity is likely due

to the absence of vacant sites for substrate activation and insufficient electron transfer between the MOF and the substrate. To improve their catalytic performances, a number of new MOFs have been synthesized and utilized as either photosensitizers or catalysts in multi component photocatalytic systems. In 2009, Mori and coworkers constructed a MOF $[Ru(p-BDC)]_n$ (BDC = terepthalic acid) as a catalyst for H_2 evolution reaction.[47]

In 2011 Lin and coworkers[47] reported a MOF photocatalyst by doping $[Re(CO)_3(5,5'-dcbpy)Cl]$ (5,5-dcbpy = 2,2'-bypyridine-5,5'-dicarboxylic acid) into a UiO-67 framework and studied its photocatalytic activity for CO_2 reduction. The MOF catalyzed CO_2 into CO in acetonitrile solution with a TON of 10.9, which is higher than parent UiO-67 complex. They believed the reason for this higher activity is site isolation of catalytic centers, which blocks decomposition routes. However, the recycled soild was inactive for CO generation. Better designs are thus needed to incorporate different components in a single MOF compound to obtain a more active and efficient catalyst.

1.4 Ruthenium Polypyridyl Complexes Containing Photocatalysts

Ruthenium polypyridyl complexes are one type of multifunctional MOFs. They have been extensively utilized in many research areas due to their excellent unique properties such as redox properties, broad absorption bands in the visible region, excited state reactivity and long-lived lifetime. Stephenson and co-workers[48] used ruthenium (II) complexes, in which ruthenium metal ion is coordinated with three 2,2-bipyridine ligands $[Ru(bpy)_3]^{2+}$ as a homogeneous photoredox catalyst for the photophysical and photochemical visible-light induced reactions. These complexes are utilized for the photocatalytic CO_2 reduction based on their broad absorption band in the visible region.[49]

The broad visible absorption band of $[Ru(bpy)_3]^{2+}$ in the visible region can be described as metal-to-ligand charge transfer (MLCT). The $[Ru(bpy)_3]^{2+}$ complex has octahedral geometry because of d^6 configuration and it has D_3 symmetry. In the ground state of ruthenium (II), all the electrons are spin paired electrons and it has the singlet state. This complex $[Ru(bpy)_3]^{2+}$ has a strong ligand field, which means there is greater separation in between an electronic states linked with the d orbitals of ruthenium. It is important because the unoccupied π^* orbitals of the bpy ligands in this complex $[Ru(bpy)_3]^{2+}$ lie in between the d-orbital states. During the photocatalysis, an electron in the ground state of metal (ruthenium) can absorb photons and transfer to ligand centered orbitals. That means an electron transfer from metal centered orbital to an orbital associated with ligand (π^* orbital). This is called metal-to-ligand charge transfer (MLCT). This particular MLCT transition was observed when this complex absorbs the 450-460 nm wavelength light in the visible region. This MLCT transfer is associated with broad absorption band in the UV-Vis spectrum of $[Ru(bpy)_3]^{2+}$.

MLCT transition reaction:

$$\mathbf{[Ru(II)(bpy)_3]^{2+} \; + photon \; \rightarrow \; [[Ru(III)(bpy)_2(bpy)^-]^{2+*}}$$
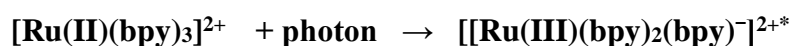
It is a redox reaction, in which ruthenium center is oxidized form Ru(II) to Ru((III), and one bipyridine ligand is reduced by gaining a negative charge and is exists in its excited state. Excited-state species are well known to engage in both oxidative and reductive chemistry.[50]

Moreover, the ruthenium polypyridyl complexes have been used as highly photoactive materials with considerably light harvesting capacities and strong photoredox

capabilities. They have been utilized as excellent photosensitizers and catalysts in homogeneous photocatalytic CO_2 reduction systems. For instance, Ishitani and coworkers[51] recently reported multinuclear ruthenium polypyridyl complexes with the fastest photocatalytic reaction rate for visible light driven reduction of CO_2.

At the same time, their derivatives $[Ru(phen)_3]^{2+}$, $[Ru(tpy)_3]^{2+}$, $[Ru(H_2dpc)_3]^{2+}$, $[Ru(5,5'-H_2dcdpy)_3]^{2+}$ were used as excellent photosensitizers due to their long-lived excited states and also have been made an important contribution to the growth of photocatalysts, photophysics, photochemistry and electrochemistry.[52] For instance, ruthenium complexes consist of 2,2'-bipyridine-4,4'-dicarboxylic acid ligands were used as photosensitizers on nano crystalline titania in the dye sensitization. These cells exhibit excellent stability with the activity of ruthenium complexes and making practical applications feasible.[53]

The major drawback of the ruthenium polypyridyl complexes is that they are photoliable in non-aqueous solvents, because of the formation of ligand photo substitution and toxic effects.[54] Another drawback of these complexes is that it is very hard to optimize both light absorption and catalytic activity at one metal center. If these complexes are immobilized onto solid materials (catalysts) to create new functional MOF materials or hybrid solids, it is possible for both isolation and recycling of the catalyst material by filtration, thus producing environmentally cleaner processes.[55]

1.4.1 Supramolecular Photocatalysts Containing Ruthenium Polypyridyl Complexes

The complexes, which contain a combined system of a photosensitizer with an active catalyst via bridging ligand, are called supramolecular complexes. In supramolecular

complexes, the photosensitizer absorbs solar light radiation and transfers electrons to the catalyst via bridging ligands.[56] In 2005, Ishitani and coworkers[57] reported the use of heteronuclear Ru-Re supramolecular catalysts for the photocatalytic reduction of CO_2 and catalytic activity was tested under the irradiation of 500 nm in presence of DMF/TEOA/BNAH solvents. However, small amounts of H_2 was produced and no HCOOH was detected. The authors believed that the electronic communication does not occur between Ru-photosensitizer and Re-catalyst. Recently, a research group[58] reported binuclear and tetranuclear Ru-Re supramolecular photocatalysts and their photocatalytic activities. The excited ruthenium in all complexes was efficiently quenched by 1-benzyl 1,4-dihydronicotinamide (BNAH). Photocatalytic activity was greatly enhanced in case of tetra and binuclear Ru-Re complexes, which is attributed to the efficient intramolecular electron transfer.

Ksuga et al.[59] synthesized Ru(II)-Ni(II) and Ru-CO complexes by using the bridging ligand of ethylene linked bisphenanthralene and observed catalytic activity of these systems. The absorption properties are dominated by Ru-moiety and no considerable contribution comes from Co or Ni catalysts respectively. The dinuclear Ru-Ni complex is less active than Ru-Co complex, but produces high amount of hydrogen during catalysis. The authors also mentioned that the coordination of CO_2 with the cobalt catalyst, which is a very interesting step and rate determining step. Thus, the efficiency of electron transfer has less effect on the overall activity of the system.

1.4.2 MOFs Containing Ruthenium Polypyridyl Complexes

Stephenson and co-workers[60] used $[Ru(bpy)_3]^{2+}$ as a photoredox catalyst for various visible light catalytic reactions and at the same time, their derivatives were used as excellent photosensitizers due to their long-lived excited states.

With this aspect, recently, researchers[61] developed a highly symmetric MOF $\{[InRu(H_2bpc)_3][(CH_3)_2NH_2]\cdot 6H_2O\}$, using photoactive $[Ru(H_2bpc)_3]^{2+}$ and indium(III) ions. The MOF exhibits a broad absorption band and displays efficient visible light photodegradation due to its long MLCT lifetime. The photocatalytic activities of this compound indicate that it is an efficient light driven photocatalyst.

Using an interpenetration strategy which can significantly increase the stability of the MOFs, Zhou, [62] Long, [63] and Mastuda[64] constructed a series of durable MOFs with $[Ru(H_2bpc)_3]^{2+}$ (4,4'-dicarboxy-2,2'-bypyridine) complex ions. It should be noted that two Ru-polypyridyl -based MOFs [65] shown similar catalytic activities for CO_2 reduction, with the penetrated MOF shown a better activity than non-penetrated.

Recently, different metal ions and organic ligands have been used to accomplish a larger surface area and distance across of the permeable channels to improve the host−guest interaction. Kato et al[66] reported five novel MOFs, synthesized from two isomeric Ru metalloligands $[(Ru (H_2bpc)_3]^{2+}$ & $[(Ru (5,5'-dcbpy)_3]^{2+}$ and divalent metal ions such as Sr^{2+}, Cd^{2+}, Mg^{2+}. All MOFs have guest-accessible porous channels and showed reversible structural transition accompanied by the adsorption/desorption of methanol or water. Their flexibilities are strongly depend on the position of the carboxyl group of metalloligand. The absorption or emission properties were characterized by the MLCT transitions.

New MOF [La$_{1.75}$(OH)$_{1.25}$(4Ru)]·6H$_2$O) (4Ru = [Ru(H$_2$bpc)$_3$]$^{2+}$) composed from ruthenium polypyridyl complex [Ru(H$_2$bpc)$_3$]$^{2+}$ and La^{3+} ions were reported by Kato et al. [67] The connection between ruthenium complex and La^{3+} ions suggests that it is an interesting framework that allow visualization of ion conductivity through MLCT emission energy.

1.5 Objective of the Research

Photochemical reduction of CO$_2$ via solar energy absorption and conversion of solar energy into chemical energy is an important solution for the increasing levels of CO$_2$ in the atmosphere. Recent research indicates that MOFs are promising photocatalysts owing to their unique structural properties such as large surface area and a finely ordered porous structures.[68] Most importantly, greater solar light absorption by organic linkers/metal ions and also efficient charge separation properties may lead to superior photocatalytic activity. Especially, researchers are utilizing ruthenium polypyridyl complexes as efficient photosensitizers for the solar energy absorption and are trying to synthesize new MOFs by the incorporation of ruthenium complexes into efficient catalysts to improve the efficiency of the photocatalysts.[69]

The main objective of this research is synthesizing new MOFs containing ruthenium polypyridyl complexes and effective catalysts (transition metals), to enhance the photocatalytic activity of MOFs.

In this thesis, I investigated the synthesis, structures, and properties of three new MOFs containing ruthenium polypyridyl complexes and 3d metals ions. Above synthesized crystal structures were characterizing by single-crystal X-ray and powder X-ray diffraction

strategies, absorption and emission properties by UV-Vis spectroscopy, IR spectroscopy and fluorescence spectroscopy. Thermal properties were determining by thermogravimetric analysis.

CHAPTER 2

MATERIALS AND METHODS

2.1 Materials

The reagents and chemicals used in this project are listed in the following table.

Table 1. Reagents & Chemicals

Chemical Name	Formula	Company Name	Grade
Ruthenium (III) chloride hydrate	$RuCl_3 \cdot H_2O$	The right chemicals	99.9%
2,2'-Bipyridine 4,4"-Dicarboxylic acid(BPC)	$C_{12}H_8N_2O4$	Alfa Acer	98%
Copper Sulfate Penta hydrate	$CuSO_4 \cdot 5H_2O$	Alfa Acer	98%
Iron(II) Chloride tetra hydrate	$FeCl_2 \cdot 4H_2O$	Acros Organics	99%
Nickle(II) nitrate hexahydrate	$Ni(NO_3)_2 \cdot 6H_2O$	Alfa Acer	98%
Water	H_2O	Deionized	
Potassium Hydroxide	KOH	Fisher Scientific	98%
Methanol/Ethanol	CH_3OH/C_2H_5OH	Aqueous solvents	95%

2.2 Hydro / Solvothermal methods

The Hydro/solvothermal methods were used in this project for the synthesis of new MOFs. The Hydro/solvothermal method is a process of crystallization in which the compounds or MOF materials are synthesized based on the solubility of a compound in presence of water or other solvents at autogenous pressure. The crystallization process is done in a PTFE (polytetrafluoroethylene-lined) vessel, which is called an autoclave. It has

two different sizes, which is 23 ml and 45ml. The autoclave is normally made of thick-lined steel cylinders, which can withstand high pressures and temperatures for an extended period of time. It is specially designed to resist corrosiveness and has good protective seals. The inside of the autoclave is coated with Teflon (polytetrafluoroethylene) or glass or Ti(Titanium) depending on the nature of the solvent used.

The sample mixtures are first placed within Teflon bags. The Teflon bags are properly sealed and kept in 45ml PTFE cup then top of the Teflon cup. Then the Teflon cup is closed with a cap. After that, the cup is placed into the autoclave. The autoclave is tightly closed with cap accessories and is placed in an oven for high temperature.[70]
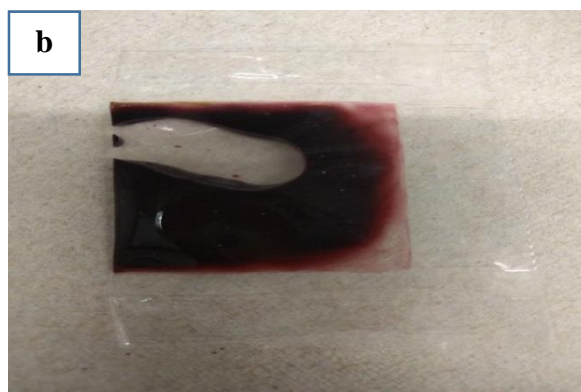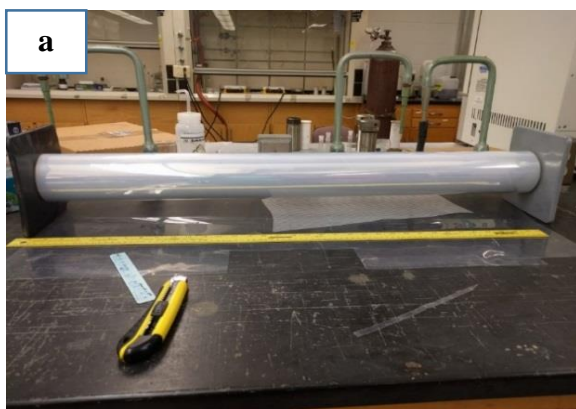
Figure 1: a) Teflon bag sheet   b) Sealed Teflon bag with sample

c) The parts of the autoclave   d) The entire setup of 45ml autoclave

2.3 Characterization Techniques

2.3.1 Powder X-ray Diffraction

Newly synthesized crystalline materials were identified by powder X-ray diffraction. X-ray diffraction technique is a versatile analytical technique for analyzing crystalline materials including metals, electronic materials, ceramics, organic compounds and polymers. All these materials may be crystals, powders, fibers and multilayer thin films which depends on the desired measurement. The instruments used for X-ray diffraction techniques are called X-ray diffractometers and these are categorized into two classes: powder X-ray and single X-ray diffractometer.[71] The operating equation, which is used for both techniques is Bragg's equation:

$$n\lambda = 2d\,sin\theta \quad \rightarrow \text{Bragg's equation}$$

Where n = reflection order(n=1,2,3…), λ = wavelength, d = distance between two parallel lattice planes and θ = an angle between incident light and a lattice plane . The diffracted intensities correlated with those peaks, which are determined by the type of atoms and its arrangement with in the crystal lattice.[72]

Powder x-ray diffraction technique is widely used rapid in analytical and non-destructive technique for the characterization of crystalline materials. Powder diffractometers are frequently used for phase identification.[73] These diffractometers are consisting of three basic units: X-ray tube, a sample holder and a detector. In powder X-ray diffractometry, X-rays are generated within a cathode tube that is under vacuum by heating a filament to product electrons and a high voltage is applied within the cathode tube. The high voltage in the tube accelerates electrons, which hit a target. Then characteristic spectra is produced.[74]

To measure the powder X-ray pattern of a compound, a newly synthesized powered sample is placed on a holder, and illuminated with a fixed wavelength X-ray beam. As sample and detector are rotated, the intensity of the reflected X-ray beam is recorded. When the geometry of the incident X-rays strikes the sample satisfies the Bragg's equation, an interference occurs and a peak in intensity occurs. Transformation of the diffraction peaks to d-spacing, allows identification of the compound because each compound has unique set of d-spacing. Typically, it is obtained by comparison of d-spacing with standard reference diffraction pattern.[75]

In this project powder X-ray diffraction pattern was obtained by using MiniFlexII Desk Top Powder X-ray diffractometer.

2.3.2 Single Crystal X-ray Diffraction

Single crystal X-ray is a non-destructive analytical technique, which gives structural information including unit-cell dimensions, bond lengths, bond angles, positions of atoms in sample, space group and details of site ordering. All these parameters can be used to verify if a structure is new or known in the literature.[76-78]

Single crystal x-ray diffractometers are mostly used to determine the structures of newly synthesized sold materials.[79] The X-ray diffraction is depending on the interference of monochromatic X-ray beam and a crystalline sample. The x-rays are produced by a cathode tube, which produces a beam of parallel monochromatic rays of approximately 1 Å wavelength strikes a single crystal. In the interaction of incident X-ray beam with a sample crystal, the crystal acts as a three-dimension grating and produces x-ray diffraction pattern, when conditions satisfy Bragg's law. This law correlates an electromagnetic radiation wavelength to the diffraction angle and the lattice spacing in a crystalline

material. These diffracted rays will be detected by the detector, then processed and counted. The single crystal used in this technique should have a regular shape without cracks and blemishes; transparency and color should be consistent.

The instrument used in this project is Bruker Quazar diffractometer for single X-ray data analysis. All data were collected on a Bruker Quazar diffractometer with an Apex II CCD detector.[80] All data were processed with SAINT software and corrected for absorption with SAD-ABS. The structures were solved by direct methods SHELXTL package and refined on F^2 by weighted full-matrix least square method. All non-hydrogen atoms were refined with anisotropic displacement parameters.[81]

Figure 2. Bruker Quazar Single X-ray Diffractometer

2.3.3 Ultraviolet-Visible Spectrophotometer

Ultraviolet-visible(UV-vis) spectroscopy is a widely used spectroscopic technique to determine the electronic structures of compounds. The ultraviolet region of the spectrum is usually considered to range from 200-400nm and the visible region from 400-800 nm. It is widely used for the identification of organic or inorganic molecules or ions, and quantitative determination of many organic, inorganic and biological species.[70] Molecules absorb UV-visible radiation and their valance electrons in that molecule are promoted from lower energy (ground) states to higher energy(excited) levels. An absorption spectrum will exhibit a number of absorption bands corresponding to transitions within the molecule.

In our project UV-Visible absorption spectra were recorded for all synthesized compounds by Varian Cary 100 UV-VIS spectrophotometer equipped with a DRA-CA-30 diffuse reflectance accessory. These spectra, provided useful information on the electronic transitions occurred within the synthesized compounds, especially metal-to-ligand charge transfer(MLCT) absorption bands for ruthenium polypyridyl complexes.

Figure 3. Cary 100 UV-Vis spectrophotometer

2.3.4 Infrared(IR) Spectroscopy

Infrared spectroscopy is an important analytical technique for the structural analysis and identification of functional groups of compounds. The basic principle of this technique is vibration of molecules in a sample can absorb specific wavelength infrared radiations. This technique can accept a wide range of sample types such as solids, liquids and gases by using various sampling accessories and every compound possesses unique spectrum decided by its structures and symmetry. Thus, IR spectroscopic technique is an important tool for structural explanation and compound identification and could be used for quantitative analysis.[70,82]

In this project, the infrared spectra were recorded from 400 to 4000cm-1 on a Perkin-Elmer Spectrum one FTIR spectrometer.

Figure 4. Perkin-Elmer Spectrum one FTIR spectrometer.

2.3.5 Fluorescence Spectroscopy

Fluorescence spectroscopy is a class of electromagnetic spectroscopy, which quantifies the intensity of photoluminescence light to permit the quantitative determination of a variety of important organic, inorganic species in trace amounts. Photoluminescence is the process in which a molecule or compound is promoted to electronic excited levels from ground state levels by the absorption of photons. All excited levels are not stable states. These excited compounds or molecules then decay back to the ground state or lower energy states by the emission of absorbed light. The emitted light by these molecules is detected. Photoluminescence process is divided into two sub classes: fluorescence and phosphorescence. The fluorescence is a process in which the electronic energy transitions are responsible for fluorescence but no change in an electron spin. Due to this, the excited states involved in fluorescence are short-lived states. But in phosphorescence, a change in an electron spin occurred, and the lifetimes of excited states are much longer.[82,83] In this project, we used a PerkinElmer L55 Luminescence Spectrometer. The possible electronic transitions occurred in between ruthenium polypyridyl complexes and catalysts were examined using fluorescence spectra.

Figure 5. PerkinElmer LS55 Fluorescence Spectrophotometer

2.3.6 Thermogravimetric analysis(TGA)

Thermogravimetric analysis is an important laboratory technique for material characterization. It is a method of thermal analysis in which the physical and chemical changes of compounds with an increasing temperature or change in mass of the compound. It includes both material transition and thermal degradation and helps in the determination of thermal stability and decomposition of material products.

In TGA the sample mass is monitored continuously as a function of temperature or time as the sample is subjected to a controlled temperature program in a controlled atmosphere (Ar, N_2). A plot of weight loss or mass percentage as a function of time is called thermogram or a thermal decomposition curve. It provides quantitative information of materials. It is limited to oxidation reactions and decomposition and to such physical processes as sublimation, vaporization and desorption.[82]

The temperature range for this technique is from ambient temperature to 1500°C. The heating and cooling rates would be selected from zero to high rates such as 200°C/min. A sample purge gas, controls the sample environment and this gas may be inert or a reactive gas pass over the sample and exits through an exhaust. Nitrogen or argon gas is utilized to prevent an oxidation of the sample.[83]

In this project, the TGA data was collected on a TA Q5000 TGA instrument. For TG analysis in this project, 10 to 25 mg powder samples of the three compounds were placed in a sample pan. Temperature program for heating of the samples is from room temperature to 700°C at 10°C/min.

Figure 6. TA Q5000 TGA instrument

CHAPTER 3

Synthesis and characterization of [Ru(H₂bpc)(Cu(bpc)(Hbpc)₂(H₂O)]·5H₂O (1)

3.1 Synthesis of [Ru(H₂bpc)(Cu(bpc)(Hbpc)₂(H₂O))]·5H₂O (1)

The synthetic reactions were done under hydrothermal conditions by using 3"×4" Teflon bags placed in 45 ml Teflon-lined stainless steel autoclave reactors. Compound **1** was prepared by heating a mixture of $RuCl_3 \cdot H_2O$ (0.0067 g, 0.030 mmol), $CuSO_4 \cdot 5H_2O$ (0.0105 g, 0.0421 mmol), 2,2'-bypyridine-4,4'-dicarboxylic acid (0.0262 g, 0.107 mmol), 0.35 mL of 0.5 M KOH, 0.5 mL methanol and 1.0 mL deionized water at 130 °C for 48 hours. After cooling to room temperature, orange red crystals (Figure 1) of compound **1** were separated from the resulting product by filtration, washed with distilled water and dried in air (59% yield based on H_2bpc).
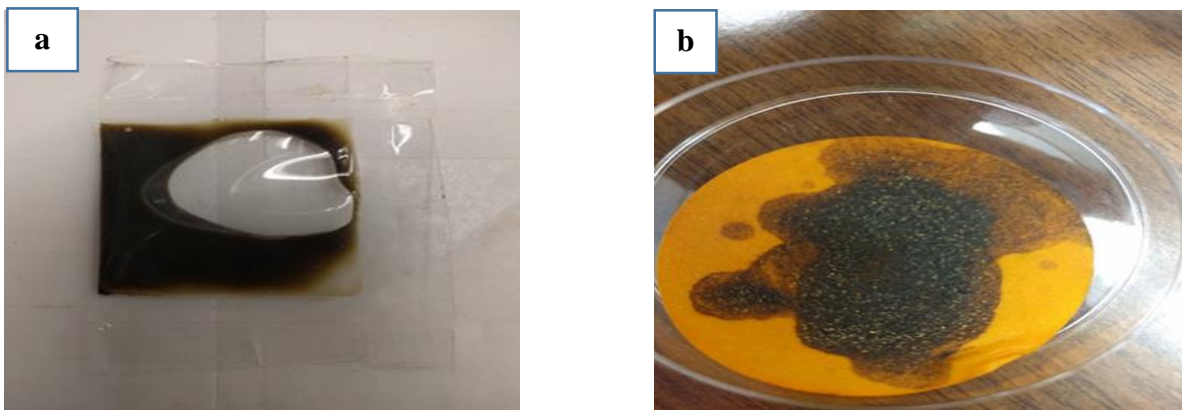
Figure 7. Before (a) & After (b) heating images of [Ru(H₂bpc)(Cu(bpc)(Hbpc)₂(H₂O))]·5H₂O (**1**)

3.2 Results & Discussions

3.2.1 Detailed Synthesis of Compound 1

Initially compound **1** was tried to be synthesized in three-steps as shown in table 1. No crystals were obtained using the three-steps method. In this method, first we tried to make

$[Ru(H_2bpc)_3]^{2+}$ in two steps (1&2) involving the addition of ligand, then ruthenium

chloride to solvents. In step 3 copper compound was added to step 2 reaction mixture in

order to make compound **1**. A two-step method was then tried. In the first step pure red

block crystals (ruthenium polypyridyl complex) were obtained by the addition of starting

materials ($RuCl_3 \cdot H_2O$ + H_2bpc ligand + HCl + H_2O). But in second step no crystals were

obtained after addition of copper sulfate pentahydrate.

Table 2. Experimental Synthesis of $[Ru(H_2bpc)(Cu(bpc)(Hbpc)_2(H_2O))]\cdot 5H_2O$ (**1**)

3-steps method	2-steps method	1-step method
H_2bpc -ligand + solvents ↓ 2hrs (130°C) (Green solution) + $RuCl_3 \cdot H_2O$ ↓ 2hrs (130°C) (Red color solution) + $CuSO_4 \cdot 5H_2O$ ↓48hrs (130°C) No crystals	$RuCl_3 \cdot H_2O$ + H_2bpc -ligand + solvents ↓ 4hrs (200°C) $Ru(bpc)_3cl_2$ - complex (pure Red black crystals) + $CuSO_4 \cdot 5H_2O$ ↓ 48 hrs (130°C) No crystals	$Rucl_3 \cdot H_2O$ + $CuSO_4 \cdot 5H_2O$ + H_2bpc- ligand + Solvents ↓(48hrs)130°C Pure red crystals

Finally, compound **1** was successfully synthesized using a single step method, as

shown in the Table 1, by changing the reaction parameters such as chemical composition,

pH, temperature and time. No crystals were obtained with pure water, methanol or ethanol

solvent. Tiny crystals were observed upon using different ratios of these solvents.

However, finally pure and large crystals were formed with 1: 0.5mL (water: methanol).

The changing of solvents effected on yield and purity of crystals. Pure crystals were formed

at 130°C and 48hrs.Upon increasing temperatures (160°C or 180°C) and changing time (24

or 72hrs) very impure (more white or blue) crystals were formed. Low yield was obtained

upon changing KOH (pH) from 0.35mL to 0.4mL, 0.5mL and above.

Table 3. Changing of parameters for the synthesis of
$[Ru(H_2bpc)(Cu(bpc)(Hbpc)_2(H_2O))]\cdot 5H_2O$

Solvents	Temp	Time	Results
Pure H_2O	130	48	No crystals
Pure CH_3OH	130	48	No crystals
Pure C_2H_5OH	130	48	No crystals
Pure DMF	130	48	No crystals
H_2O- 2 & 4 ml	130	48	Red & less white crystals
CH_3OH-1 & 1.5 ml	130	48	Less red & more white crystals
H_2O - 3ml	160	48	Equal red & white crystals
H_2O- 1ml & CH_3OH - 0.5 ml	**130**	**48**	**Pure Red crystals**
H_2O- 1ml & CH_3OH - 0.5 ml	130	72	Blue, white crystals
H_2O- 3ml & C_2H_5OH - 1.5ml	130	48	More white crystals
H_2O- 1ml & CH_3OH- 1ml	180	24	More white crystals
H_2O- 1ml & C_2H_5OH- 0.5ml	160	72	Pure Red crystals

3.2.2 Crystal structure of $[Ru(H_2bpc)(Cu(bpc)(Hbpc)_2(H_2O))]\cdot 5H_2O$ (1)

Single crystal X-ray diffraction intensities for compound **1** were collected on a Nonius

kappa CCD diffractometer equipped with graphite monochromated Mo Kα radiation with

a radiation wavelength of 0.71073Å. The structure was solved by direct methods and

refined on F^2 by weighted full matrix least squares using the SHELXTL-97 program

package. Non-hydrogen atoms were refined with anisotropic displacement parameters. The

organic hydrogen atoms were found in difference maps but subsequently placed at

calculated positions and refined using a riding model. The final wR_2 (all data) = 0.1233, final R_1 = 0.0481. Crystal data and relevant details of compound **1** structure determinations are summarized in the following table 4 and selected bond lengths & bond angles are given in the table 5.

Table 4. Crystal data and structure refinements for [Ru(H$_2$bpc)(Cu(bpc)(Hbpc)$_2$(H$_2$O))]·5H$_2$O (**1**)

Empirical formula	C$_{48}$ H$_{27}$ Cu N$_8$ O$_{22.50}$ Ru
Formula weight	1240.39
Temperature	295 K
Wavelength	0.71073 Å
Crystal system	triclinic
Space group	p-1
Unit cell dimensions	a = 11.895(5) Å a= 80.80(4)°.
	b = 14.885(6) Å b= 68.39(2)°.
	c = 16.087(9) Å g = 89.74(3)°.
Volume	2610(2) Å^3
Z	2
Density (calculated)	1.579 Mg/m^3
Absorption coefficient	0.788 mm^{-1}
F(000)	1248
Crystal size	0.20 x 0.16 x 0.02 mm^3
Theta range for data collection	1.38 to 27.50°.
Index ranges	-15<=h<=15, -19<=k<=19, -20<=l<=20
Reflections collected	44043
Independent reflections	11768 [R(int) = 0.0378]
Completeness to theta = 27.50°	98.1 %
Max. and min. transmission	0.9883 and 0.8584
Refinement method	Full-matrix least-squares on F^2
Data / restraints / parameters	11768 / 0 / 765
Goodness-of-fit on F^2	1.088
Final R indices [I>2sigma(I)]	R$_1$ = 0.0390, wR$_2$ = 0.1176
R indices (all data)	R$_1$ = 0.0481, wR$_2$ = 0.1233
Largest diff. peak and hole	0.982 and -0.542 e.Å$^-$

Table 5. Selected Bond lengths and Bond angles of
$[Ru(H_2bpc)(Cu(bpc)(Hbpc)_2(H_2O))]\cdot5H_2O$

Bond lengths [Å]		Bond angles [°]	
Ru(01)-N(3)	2.046(2)	N(3)-Ru(01)-N(8)	171.81(9)
Ru(01)-N(8)	2.048(2)	N(3)-Ru(01)-N(7)	94.88(10)
Ru(01)-N(7)	2.049(3)	N(8)-Ru(01)-N(7)	78.66(10)
Ru(01)-N(5)	2.052(3)	N(3)-Ru(01)-N(5)	91.91(10)
Ru(01)-N(6)	2.066(3)	N(8)-Ru(01)-N(5)	95.04(10)
Ru(01)-N(4)	2.078(2)	N(7)-Ru(01)-N(5)	171.17(9)
Cu(02)-O(13)#1	1.938(2)	N(3)-Ru(01)-N(6)	99.35(10)
Cu(02)-O(7)	1.949(2)	N(8)-Ru(01)-N(6)	86.28(10)
Cu(02)-N(1)	2.000(3)	N(7)-Ru(01)-N(6)	94.59(10)
Cu(02)-N(2)	2.014(3)	N(5)-Ru(01)-N(6)	78.70(10)
Cu(02)-O(1W)	2.248(3)	N(3)-Ru(01)-N(4)	78.73(10)
O(1)-C(11)	1.302(4)	N(8)-Ru(01)-N(4)	95.80(10)
O(1)-H(1A)	0.8200	N(7)-Ru(01)-N(4)	87.20(10)
O(2)-C(11)	1.203(5)	N(5)-Ru(01)-N(4)	99.68(10)
O(3)-C(12)	1.234(4)	N(6)-Ru(01)-N(4)	177.49(9)
O(4)-C(12)	1.245(4)	O(13)#1-Cu(02)-O(7)	90.27(11)
O(5)-C(23)	1.289(4)	O(13)#1-Cu(02)-N(1)	172.60(11)
O(5)-H(5)	0.8200	O(7)-Cu(02)-N(1)	95.85(11)
O(6)-C(23)	1.221(5)	O(13)#1-Cu(02)-N(2)	93.11(11)
O(7)-C(24)	1.262(4)	O(7)-Cu(02)-N(2)	175.08(11)
O(8)-C(24)	1.231(4)	N(1)-Cu(02)-N(2)	80.53(11)
O(9)-C(35)	1.198(5)	O(13)#1-Cu(02)-O(1W)	92.22(13)
O(10)-C(35)	1.306(5)	O(7)-Cu(02)-O(1W)	89.48(11)
O(10)-H(10A)	0.8200	N(1)-Cu(02)-O(1W)	92.01(14)
O(11)-C(36)	1.302(4)	N(2)-Cu(02)-O(1W)	93.96(12)
O(11)-H(11)	0.8200	O(2)-C(11)-O(1)	124.5(4)
O(12)-C(36)	1.200(4)	O(2)-C(11)-C(3)	123.0(3)
O(13)-C(47)	1.267(4)	O(1)-C(11)-C(3)	112.4(3)
O(14)-C(47)	1.213(4)	O(3)-C(12)-O(4)	123.8(3)

Symmetry transformations used to generate equivalent atoms:

#1 x-1,y,z   #2 x+1,y,z
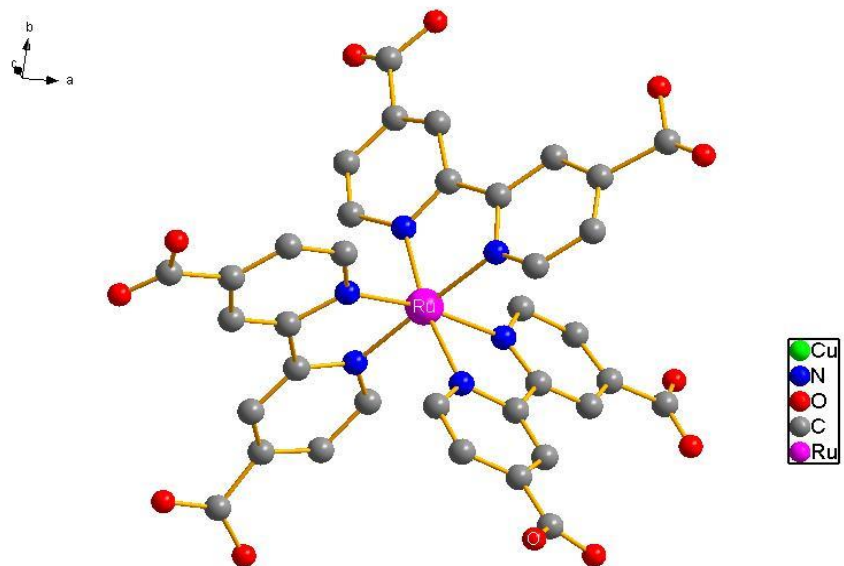
Figure 8. Geometry of [Ru(H₂bpc)(Hbpc)₂] in compound **1**
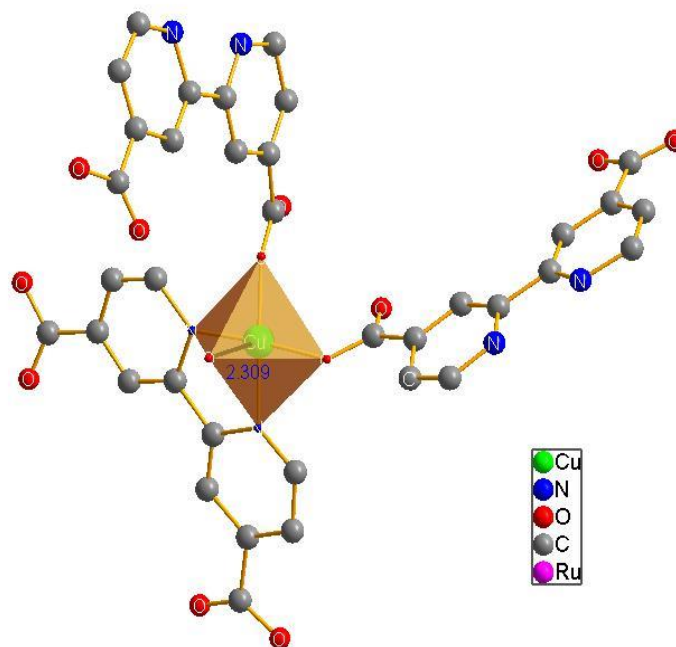
Figure 9. Geometry of [Cu(Hbpc)₂(bpc)] in

[Ru(H₂bpc)(Cu(bpc)(Hbpc)₂(H₂O)]·5H₂O (**1**).

Single crystal X-ray diffraction analysis reveals that compound **1** crystallizes in the triclinic space group $P\bar{1}$. The asymmetric unit contains one Ru(II), one Cu(II) ion, two Hbpc$^-$ ligand anions, one bpc^{2-} ion, one H$_2$bpc ligand molecule, one coordinated water and several lattice water molecules. Each chiral ruthenium (II) center bonds to three organic ligands through Ru-N bonds to form an octahedral coordination geometry [Ru(H$_2$bpc)(Hbpc)(bpc)]$^-$(Fig 8). The Ru-N bond lengths are in the range of 2.046(2)-2.078(2) Å. The Ru(II) complex ions are bridged by [Cu(Hbpc)(H$_2$O)]$^+$ ions into a one-dimensional (1D) zigzag chain running along the *a* direction (Fig 10). The Cu(II) ions in the 1D chain adopt a square-pyramidal geometry [Cu(Hbpc)(bpc)$_2$(H$_2$O)]$^-$ with two oxygen atoms from two carboxylate groups, one oxygen atom from a water molecule and two nitrogen atoms of a Hbpc ligand(Fig 9).
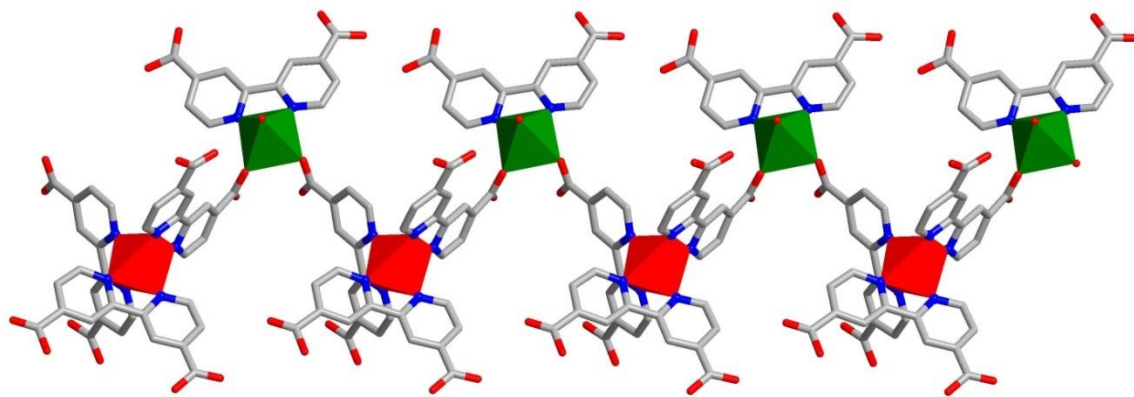
Figure 10. The wire and polyhedra representation of the one-dimensional chain in compound [Ru(H$_2$bpc)(Cu(bpc)(Hbpc)$_2$(H$_2$O)]·5H$_2$O (**1**).

The Cu-O bond length involving water in the apical position is much longer (2.248(3)Å) than those involving carboxylate oxygen (1.938(2) and 1.949(2)Å). A water molecule located beneath the basil plane of pyramid has a Cu···O distance of 3.435(2)Å. The Cu-N bond lengths are in the normal range (2.000(3) and 2.014(3)Å). The coordinate water molecule can be potentially removed to give a MOF with open coordination sites,

which are considered as key factors in the application of MOFs.[84] It is interesting to note that there are three forms of the H_2bpc ligand molecule in the compound: H_2bpc, $Hbpc^-$ and bpc^{2-}. This can be confirmed by the charge balance of the counter ions in the chemical formula and IR spectroscopy of the solid (Fig 14).
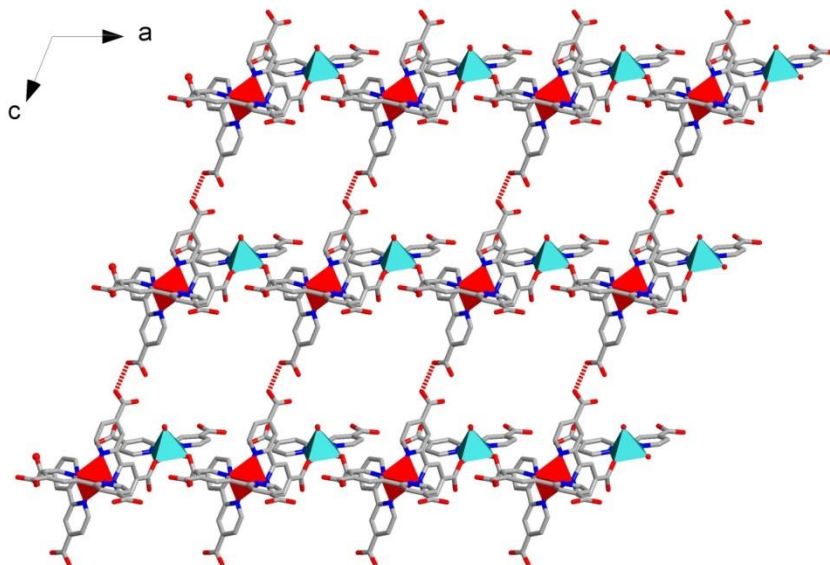
Figure 11. The two-dimensional net work formed by hydrogen bonding between the one- dimensional chain in compound $[Ru(H_2bpc)(Cu(bpc)(Hbpc)_2(H_2O))]\cdot5H_2O$ (**1**).

As shown in Fig 14, the band at 1705 cm^{-1} can be assigned to the stretching vibration of C=O of −COOH group, while the double bands at 1610-1646 cm^{-1} are the vibrations of carboxylate groups −COO$^-$. In terms of the bonding modes, there are two types of bpc ligands: one type is the bridging ligand, which links copper ions and ruthenium ions, and one type is the terminal ligand, which is chelating to only to either a Ru(II) or a Cu(II) ion. The 1D chains in **1** are connected by hydrogen bonds between bpc ligands on Ru to form a 2D layered structures (fig 11) which are stacking along the *b* direction.

3.2.3 Powder X-ray Diffraction

The phase purity of this compound was confirmed by powder X-ray diffraction analysis. It was confirmed by comparing the powder X-ray diffraction pattern of the synthesized sample (compound 1) and the stimulated pattern from the crystal structure. Compound **1** is pure product based on the agreement of this PXRD diffraction patterns and the stimulated patterns (fig 12).
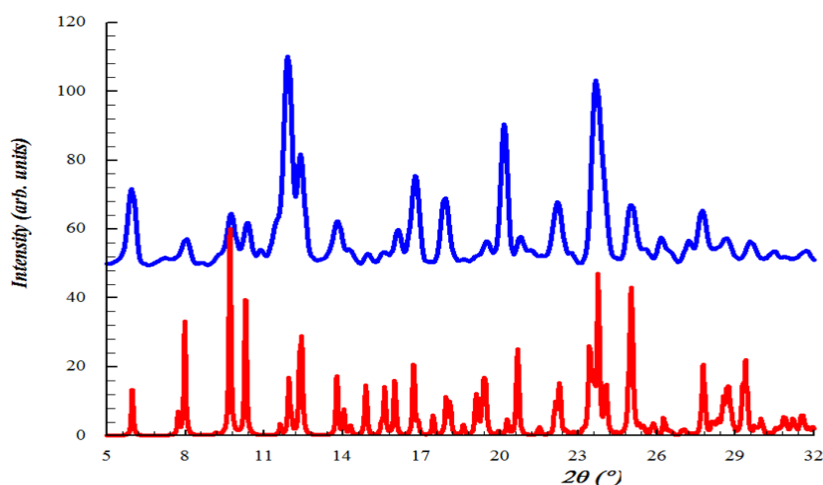
Figure 12. Powder X-ray diffraction patterns of[Ru(H₂bpc)(Cu(bpc)(Hbpc)₂(H₂O))]·5H₂O

3.2.4 UV-Visible spectroscopy
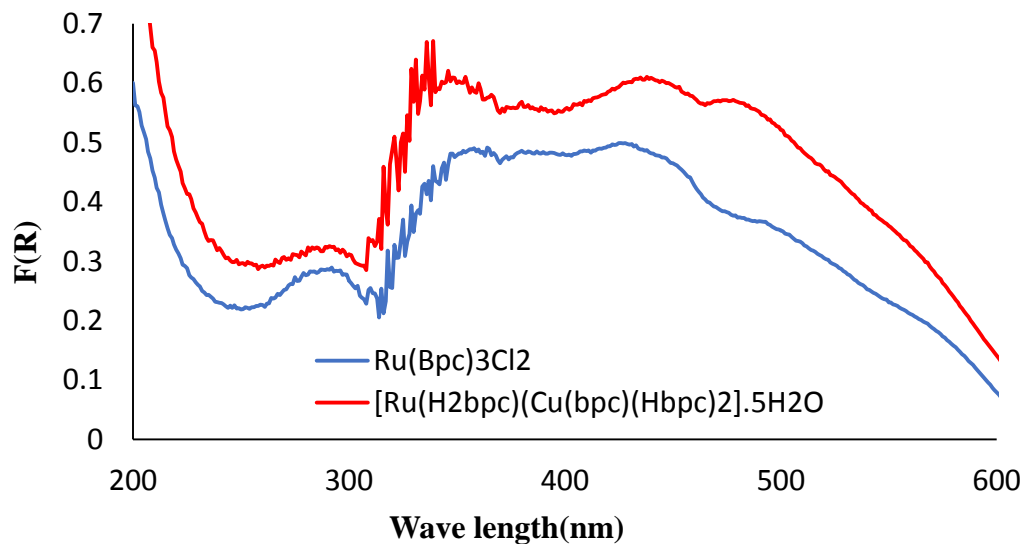
Figure 13. The UV-vis spectrum of compound 1 and [Ru(bpc)$_3$Cl$_2$]

Figure 13. displays UV-vis absorption spectra of [Ru(bpc)$_3$]Cl$_2$] and compound **1.** The UV-vis spectra results indicates the electronic properties of the synthesized compound. Compound **1**shown the characteristic absorption band of [Ru(H$_2$bpc)$_3$]$^{+2}$ with two peaks, at 440 and 480nm in the visible region. These bands can be attributed to the metal-to-ligand charge transfer(MLCT) transition in which an electron is located in ruthenium-based orbitals are promoted into ligand(bpc)-centered π^* orbitals. These absorption bands shifted to red compared to the discrete [Ru(H$_2$bpc)$_3$]$^{+2}$ which shows a broad band at 427nm. These are comparable to other MOFs containing [Ru(bpc)$_3$]$^{n+}$. These shifts are believed to be caused by the coordination to Cu^{+2} through carboxylate ligand. Both compounds(Ruthenium complex and compound **1**) shown similar absorption spectrums which indicates compound **1** is orginated from Ruthenium polypyridyl ligand [Ru(bpc)$_3$Cl$_2$].

The UV-absorption band was located at 248 nm corresponds to a ligand centered π π^*transition of bpc (2,2'-bipyridine-4,4'-dicarboxylate) ligand which is overlapped by MLCT absorption band. These changes of charge transitions in compound **1** clearly indicates that the electronic communication occurred between ruthenium polypyridyl complex and copper catalyst.

3.2.5 FTIR spectra

The FTIR spectra results shown major stretching vibration bands in compound **1**.The vibration band around 3084 cm^{-1} which is the characteristic absorption band of –OH group strecthing vibration of bpc ligand and water molecule. Another absorption band observed around 1703 cm^{-1} which is attributed to the caboxyl group (C=O) of bpc ligand. Several

absorption bands located between 1400-1900 cm^{-1} which corresponds to the characteristic stretching vibrations of bpc(2,2' bypyridine-4,4'-dicarboxylate) ligands.
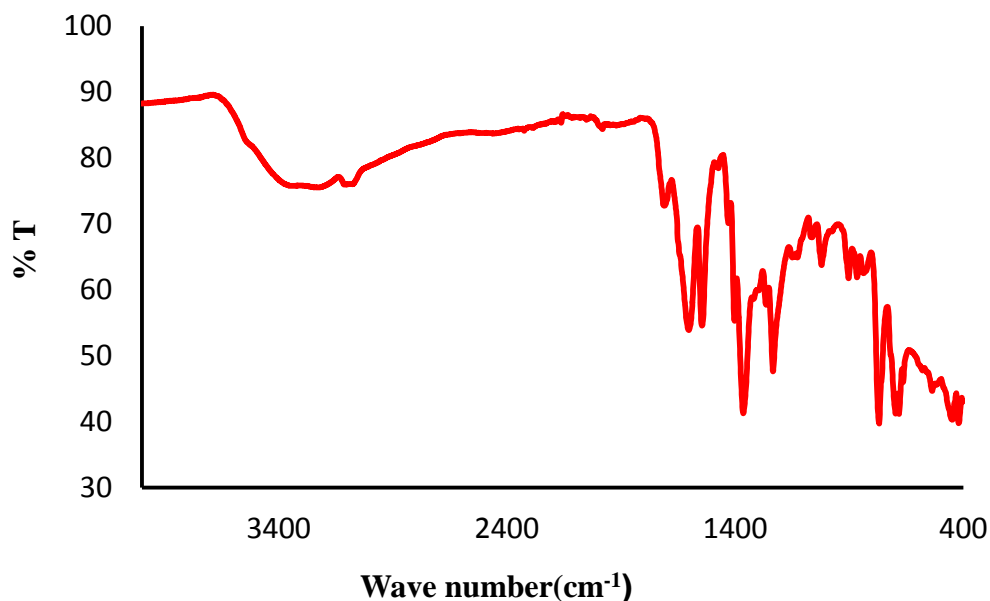
Figure 14. FTIR spectra of [Ru(H$_2$bpc)(Cu(bpc)(Hbpc)$_2$(H$_2$O))]·5H$_2$O (**1**)

3.2.6 Flourescence spectra

The fluorescence spectra of ruthenium polypryridyl complex and compound **1** was examined at room temparature and emission spectra for both compounds is depicted below. Upon excitation at the λ$_{max}$ (440 nm) of the MLCT band of the ruthenium polypyridine complex, an emission centered band was observed at 626 nm. For compound **1** an emission band was observed with lower intensity around 601-606 nm upon excitation at λ$_{max}$ (450nm) due to the coordination of copper catalyst with ruthenium polypyridyl complex. The emission bands for both compounds can be attributed to the emission of energy from triplet MLCT excited state ruthenium to the singlet ground state.
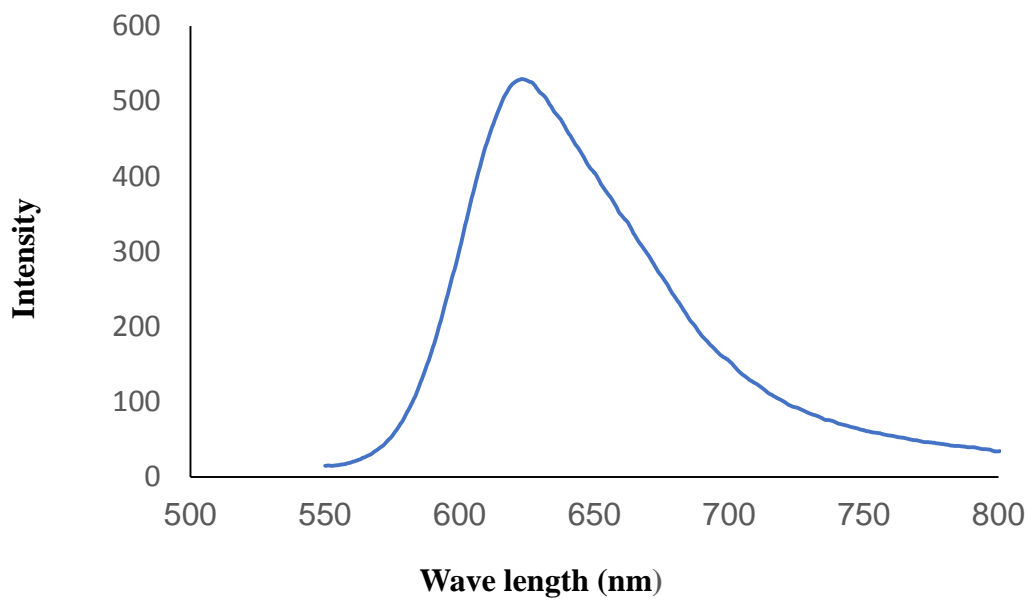
Figure 15. Fluorescence spectra of ruthenium polypyridyl complex
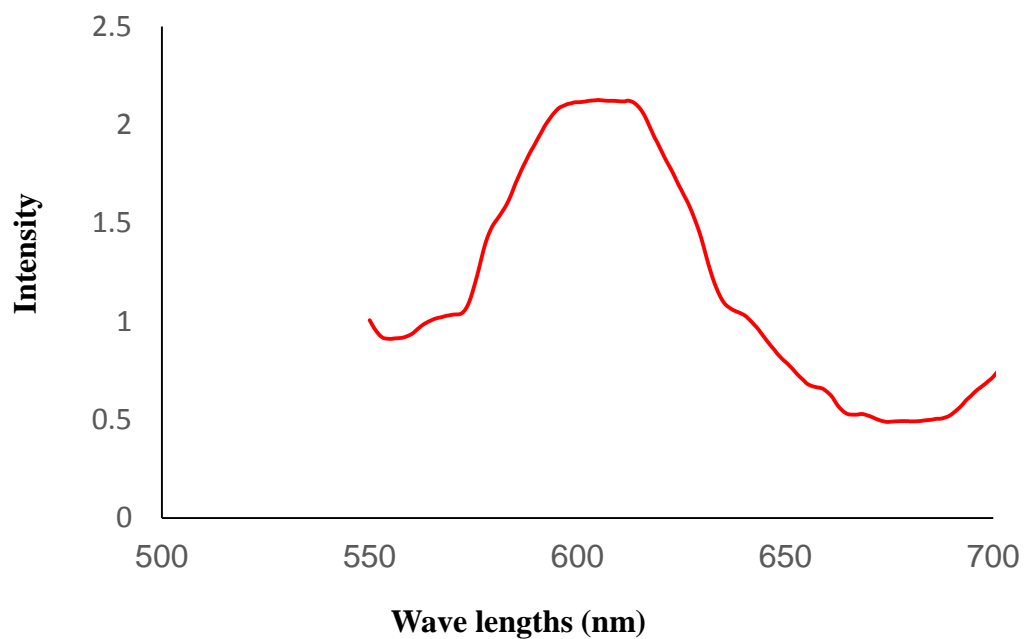
Figure 16. Fluorescence spectra of compound **1**

3.2.7 Thermogravimetric Analysis (TGA)
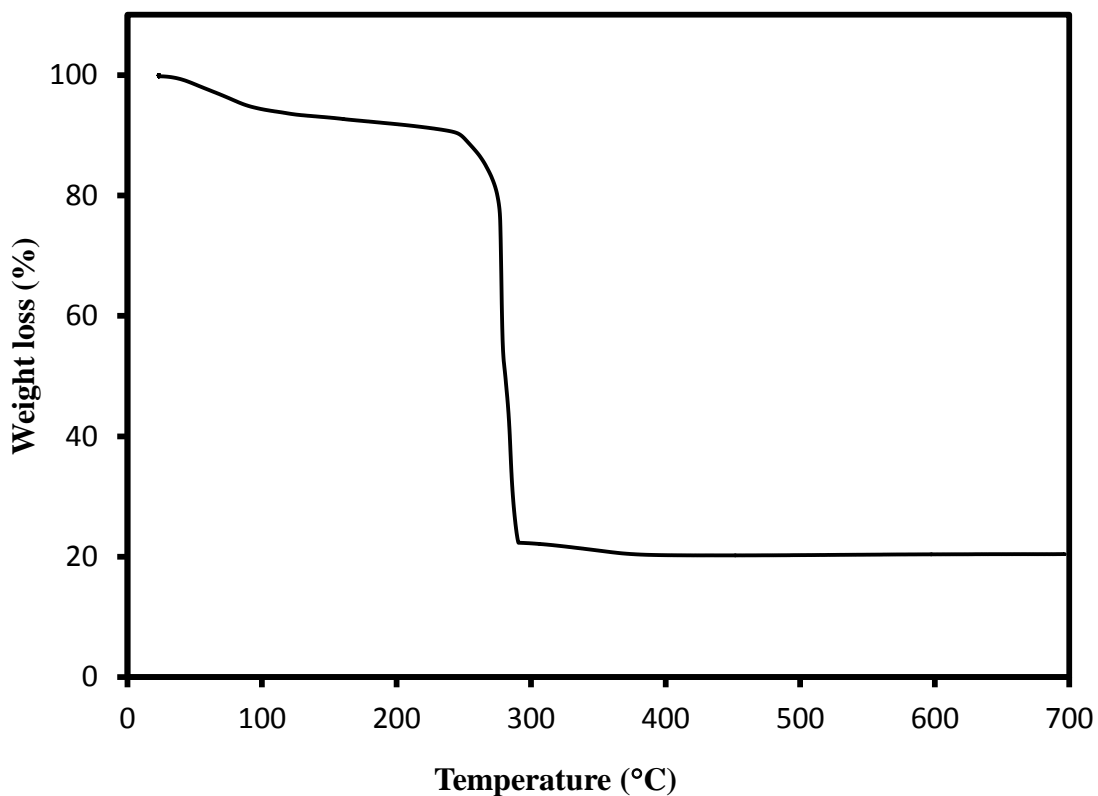
Figure 17. TGA plot of compound **1**

Thermal stability or structural ability of compound **1** was investigated on powder samples under N_2 atmosphere in the temparature range between 24°C-700°C. The TG graph of compound **1** exhibits a two step weight loss of approximately 8.7% weight loss, which is attributed to the loss of absorbed moisture or water molecules upon heating 40°C -200°C(calculated 8.77%) . And 71% of weight loss was observed because of the decomposition of bpc ligand molecules upon heating from 230°-720°C(calculated 75.3%).

3.2.8 Magnetic Properties of Compound 1
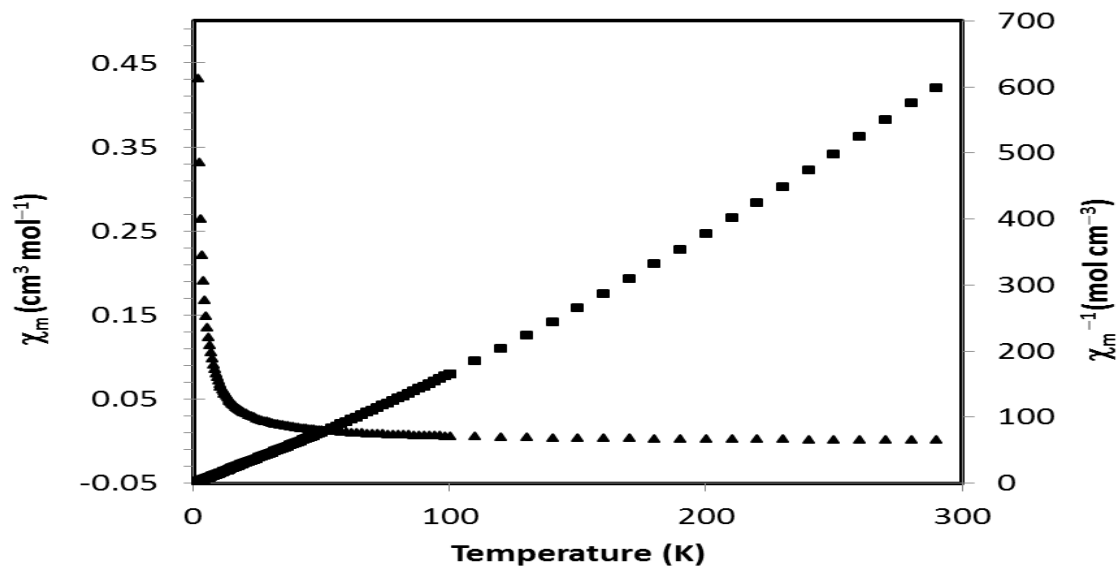
Figure 18. Magnetic susceptibility versus temperature for compound
$[Ru(H_2bpc)(Cu(bpc)(Hbpc)_2(H_2O))]{\cdot}5H_2O$ (**1**).

The magnetic susceptibilities of **1** (Figure 18) shows a strong temperature dependence and is consistent with one Cu(II) ion per formula unit. The data at higher temperatures could be fitted to a Curie−Weiss expression with $\theta = 34$ K and C = 0.43 emu·mol^{-1}·K. The positive θ value suggests the presence of ferromagnetic interactions between the copper ions. The magnetic moment (μ_{eff}) at 300 K per mole of copper ion is 1.96 μ_B, in agreement with those reported for other Cu(II) compounds.

3.3 Conclusion

In summary, using Ru(II) polypyridyl complexes as building units and transition metal ions as linkers, we have successfully synthesized a 1D metal-organic framework with two different metal centers. Diffraction intensities for **1** were collected on a Nonius kappa CCD diffractometer equipped with graphite monochromated Mo Kα radiation with a radiation wavelength of 0.71073Å. The structure was solved by direct methods and refined on F^2 by weighted full matrix least squares using the SHELXTL-97 program package. Non-hydrogen atoms were refined with anisotropic displacement parameters. The organic hydrogen atoms were found in difference maps but subsequently placed at calculated positions and refined using a riding model. The Ru(II) metal centers show MLCT bands centered around 440 and 480 nm, and emit fluoresce at 610 nm. The 87% weight loss was observed upon heating from 40°C -200°C and 71% weight loss from 230-720^{0}C due to evaporation of moisture and decomposition of ligand. The Cu(II) centers show ferromagnetic interactions with $\theta = 34$ K and C = 0.43 emu·mol^{-1}·K for its Curie−Weiss equation.

CHAPTER 4

Synthesis and Characterization of [Ru(H₂bpc)Fe(Hbpc)₂(bpc)(H₂O)₂]·6H₂O (2)

Synthesis and Characterization of $[Ru(H_2bpc)Fe(Hbpc)_2(bpc)(H_2O)_2]·6H_2O$ **(2)**

4.1 Synthesis of $[Ru(H_2bpc)Fe(Hbpc)_2(bpc)(H_2O)_2]·6H_2O$ (2)

Compound **2** was synthesized under hydrothermal conditions using 3"×4" Teflon bags that were placed in 45 ml Teflon-lined stainless steel autoclave reactors. A typical reaction is as follow: $RuCl_3·H_2O$ (0.0067 g, 0.032mmol) was added to 1 mL aqueous solution of $FeCl_2·4H_2O$ (0.0083 g, 0.042 mmol). The resulting red mixture was mixed with 0.35mL of 0.5M KOH followed by the addition of 0.5 mL ethanol and 2,2'-bypyridine-4,4'-dicarboxylic acid ligand (0.0267 g, 0.10 mmol). The mixture was then transferred to a Teflon bag, sealed and placed in a 45 mL autoclave which was heated in an oven at 160°C for 72 hours. After the autoclave was cooled to room temperature naturally, red crystals were filtered and washed with deionized water, and dried in air (yield 64%).
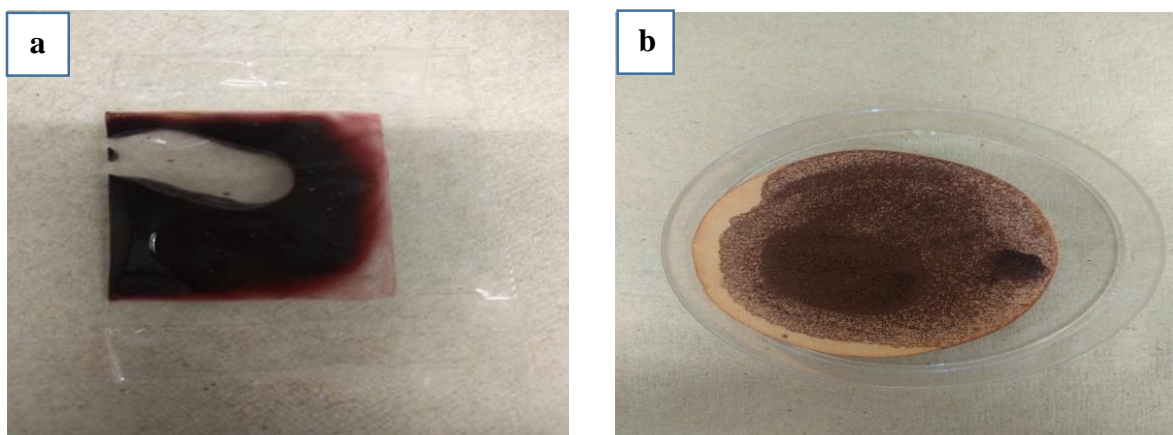
Figure 19. Before (a) & After (b) heating images of $[Ru(H_2bpc)(Fe(Hbpc)_2(bpc)(H_2O)_2)]$

4.2 Results & Discussion

4.2.1 Synthesis of $[Ru(H_2bpc)Fe(Hbpc)_2(bpc)(H_2O)_2]·6H_2O$ (2)

During the synthesis of **2**, the reaction parameters were changed as following. Pure red crystals of compound **2** were obtained by the reaction of starting materials with appropriate solvents (H_2O-1mL, ethanol-0.5mL& 0.5MKOH-0.35mL) at 160°C & 72 hrs as shown in the Table 6. Changing ratios of these solvents effected the yield & purity of crystals. Increasing temperatures (160°C &180°C) and changing time (48 &72hrs) affect the shapes of the crystals. Low yield was obtained upon changing KOH (pH) from 0.35mL to 0.4mL, 0.5mL and above.

Table 6. Changed reaction parameters for the synthesis of compound **2**

Solvents	Temp	Time	Results
H_2O-1ml, CH_3OH-0.5 ml &KOH-0.35ml	130&160°C	48 & 72 hrs	Impure crystals
H_2O-3ml, CH_3OH-0.5 ml &KOH-0.35ml	130&160°C	48 & 72 hrs	Impure crystals
H_2O-1ml ,CH_3OH-1 ml &KOH-0.4ml	130&160°C	48 &72 hrs	Impure crystals
H_2O-1ml , CH_3OH-1ml &KOH-0.45ml	130&160°C	48 &72 hrs	Impure crystals
H_2O-1ml & C_2H_5OH-0.5ml&KOH-0.35ml	**160°C**	**72 hrs**	**pure crystals**
H_2O-3ml & C_2H_5OH-0.5 ml &KOH-0.35ml	130&160°C	72 hrs	Impure crystals
H_2O-1ml & C_2H_5OH-1ml &KOH-0.35ml	160°C	72hrs	Impure crystals
H_2O-1ml & C_2H_5OH-0.5 ml &KOH-0.35ml	180°C	48 & 72 hrs	Impure crystals

4.2.2 Crystal structure of compound 2

Table 7. Crystal data and structure refinements for [Ru(H$_2$bpc)Fe(Hbpc)$_2$(bpc)(H$_2$O)$_2$]·6H$_2$O(**2**)

Empirical formula	C$_{48}$H$_{44}$FeN$_8$O$_{24}$Ru
Formula weight	1273.8
Temperature	295(2) K
Wavelength	0.71073 Å
Crystal system	Triclinic
Space group	P-1
Unit cell dimensions	a = 11.814(5) Å a= 97.53(3)°.
	b = 14.806(7) Å b= 110.791(17)°.
	c = 16.016(8) Å g = 91.08(2)°.
Volume	2590(2) Å^3
Z	2
Density (calculated)	1.316 Mg/m^3
Absorption coefficient	1.181 mm^{-1}
F(000)	1016
Crystal size	0.11 x 0.10 x 0.05 mm^3
Theta range for data collection	1.39 to 29.40°.
Index ranges	-16<=h<=16, -20<=k<=20, -21<=l<=22
Reflections collected	35652
Independent reflections	13206 [R(int) = 0.0507]
Completeness to theta = 29.40°	92.3 %
Absorption correction	None
Max. and min. transmission	0.9433 and 0.8811
Refinement method	Full-matrix least-squares on F^2
Data / restraints / parameters	13206 / 0 / 703
Goodness-of-fit on F^2	1.051
Final R indices [I>2sigma(I)]	R1 = 0.0928, wR2 = 0.2885
R indices (all data)	R1 = 0.1120, wR2 = 0.3054
Largest diff. peak and hole	3.983 and -1.710 e.Å^{-3}

Table 8. Selected Bond lengths and Bond angles of
[Ru(H$_2$bpc)Fe(Hbpc)$_2$(bpc)(H$_2$O)$_2$]·6H$_2$O (**2**)

Bond lengths[Å]		Bond angles [°]	
Ru(1)-N(6)	1.989(5)	N(6)-Ru(1)-N(5)	81.02(19)
Ru(1)-N(5)	1.995(5)	N(6)-Ru(1)-N(7)	178.75(18)
Ru(1)-N(7)	2.008(4)	N(5)-Ru(1)-N(7)	98.74(19)
Ru(1)-N(3)	2.013(4)	N(6)-Ru(1)-N(3)	93.41(18)
Ru(1)-N(9)	2.021(5)	N(5)-Ru(1)-N(3)	172.33(19)
Ru(1)-N(4)	2.031(4)	N(7)-Ru(1)-N(3)	86.94(18)
Fe(2)-O(16)	2.037(4)	N(6)-Ru(1)-N(9)	99.46(19)
Fe(2)-O(14)	2.048(4)	N(5)-Ru(1)-N(9)	92.32(19)
Fe(2)-O(17)	2.094(5)	N(7)-Ru(1)-N(9)	79.31(18)
Fe(2)-N(2)	2.127(5)	N(3)-Ru(1)-N(9)	93.80(18)
N(1)-C(45)	1.331(8)	N(6)-Ru(1)-N(4)	86.01(18)
N(1)-C(37)	1.340(7)	N(5)-Ru(1)-N(4)	94.46(19)
N(1)-Fe(2)	2.145(5)	N(7)-Ru(1)-N(4)	95.23(18)
O(11)-C(40)	1.272(8)	N(3)-Ru(1)-N(4)	79.83(17)
O(6)-C(44)	1.295(8)	N(9)-Ru(1)-N(4)	171.88(16)
O(9)-C(26)	1.264(7)	O(16)-Fe(2)-O(14)	96.0(2)
O(10)-C(26)	1.241(7)	O(16)-Fe(2)-O(17)	91.4(2)
O(3)-C(18)	1.243(7)	O(14)-Fe(2)-O(17)	91.5(2)
O(5)-C(44)	1.219(8)	O(16)-Fe(2)-N(2)	169.9(2)
O(4)-C(18)	1.241(7)	O(14)-Fe(2)-N(2)	92.68(18)
O(1)-C(46)	1.286(9)	O(17)-Fe(2)-N(2)	93.5(2)
O(12)-C(40)	1.221(9)	O(16)-Fe(2)-N(1)	95.1(2)
O(7)-C(48)	1.278(11)	O(14)-Fe(2)-N(1)	167.0(2)
O(2)-C(46)	1.212(10)	O(17)-Fe(2)-N(1)	95.1(2)
O(8)-C(48)	1.213(11)	C(45)-N(1)-C(37)	119.8(5)
O(14)-C(25)	1.267(7)	C(45)-N(1)-Fe(2)	123.6(4)
O(13)-C(25)	1.230(8)	C(37)-N(1)-Fe(2)	116.3(4)
O(16)-C(71)	1.267(8)	N(2)-Fe(2)-N(1)	75.72(18)

Symmetry transformations used to generate equivalent atoms:

#1 x-1,y,z   #2 x+1,y,z
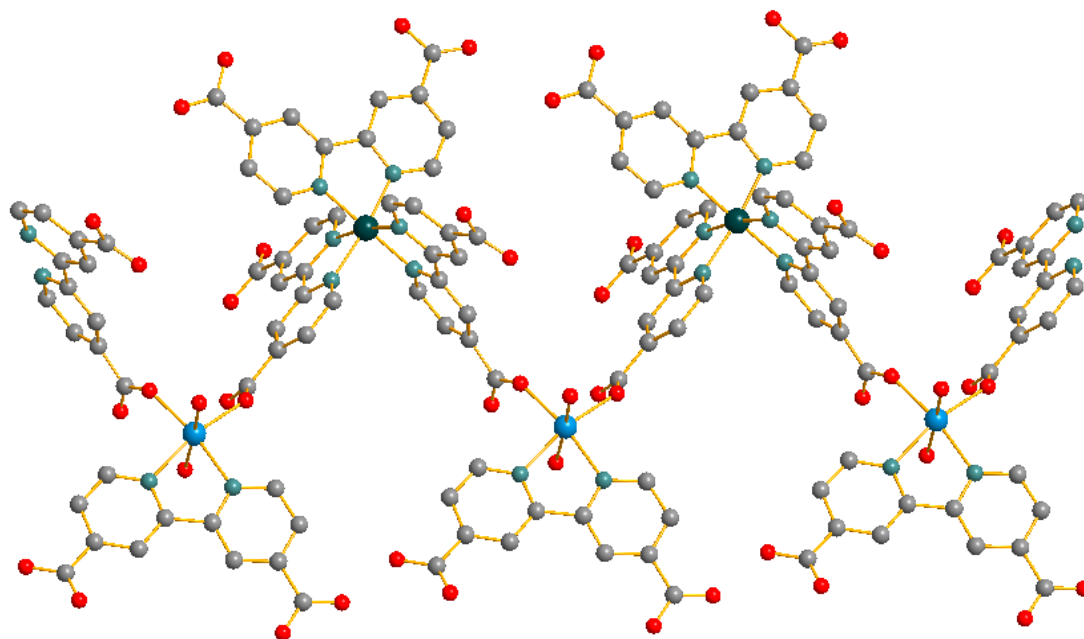
Figure 20. One-dimensional structure of [Ru(H$_2$bpc)Fe(Hbpc)$_2$(bpc)(H$_2$O)$_2$]·6H$_2$O (**2**)

Single crystal X-ray diffraction analysis reveals that compound **2** crystallizes in the triclinic space group $P\bar{1}$. The asymmetric unit contains one Ru(II), one Fe(II) ion, two Hbpc$^-$ ligand anions, one bpc^{2-} ion, one H$_2$bpc ligand molecule, two coordinated water and several lattice water molecules. Each chiral ruthenium(II) center bonds to three organic ligands through Ru-N bonds to form an octahedral coordination geometry [Ru(H$_2$bpc)(Hbpc)(bpc)]$^-$. The Ru-N bond lengths are in the range of 1.989 Å -2.031 Å. The Ru(II) complex ions are bridged by [Fe(Hbpc)(H$_2$O)]$^+$ ions into a one-dimensional (1D) zigzag chain running along the *a* direction (Fig 20). The Fe(II) ions in the 1D chain adopt a octahedral geometry [Fe(Hbpc)(bpc)$_2$(H$_2$O)]$^-$ with two oxygen atoms from two carboxylate groups, two oxygen atoms from two water molecules and two nitrogen atoms of a Hbpc ligand. The Fe^{2+} crystal unit is coordinated with two water molecules via two different Fe-O bonds. The two Fe-O bond lengths involving water has similar lengths

(2.094Å & 2.048 Å) to the carboxylate oxygen (1.998(4) and 2.037(4) Å). The Fe-N bond

lengths are in the normal range (2.127(5) and 2.145(5) Å). The coordinate water molecules

can be potentially removed to give a MOF with open coordination sites, which are

considered as key factors in the application of MOFs. It is interesting to note that there are

three forms of the H_2bpc ligand molecule in the compound: H_2bpc, $Hbpc^-$ and bpc^{2-}. This

can be confirmed by the charge balance of the counter ions in the chemical formula and IR

spectroscopy of the solid (Fig 22).

In Compound **2,** the Fe^{2+} unit-possess octahedral geometry with two distorted axial

positioned Fe-O bonds, whereas copper unit in compound **1** has square-pyramidal

geometry with one Cu-O bond. The Fe-O bonds are shorter than Cu-O bond involving

water molecules, because of John-teller distortion.

4.2.3 UV-Visible spectroscopy
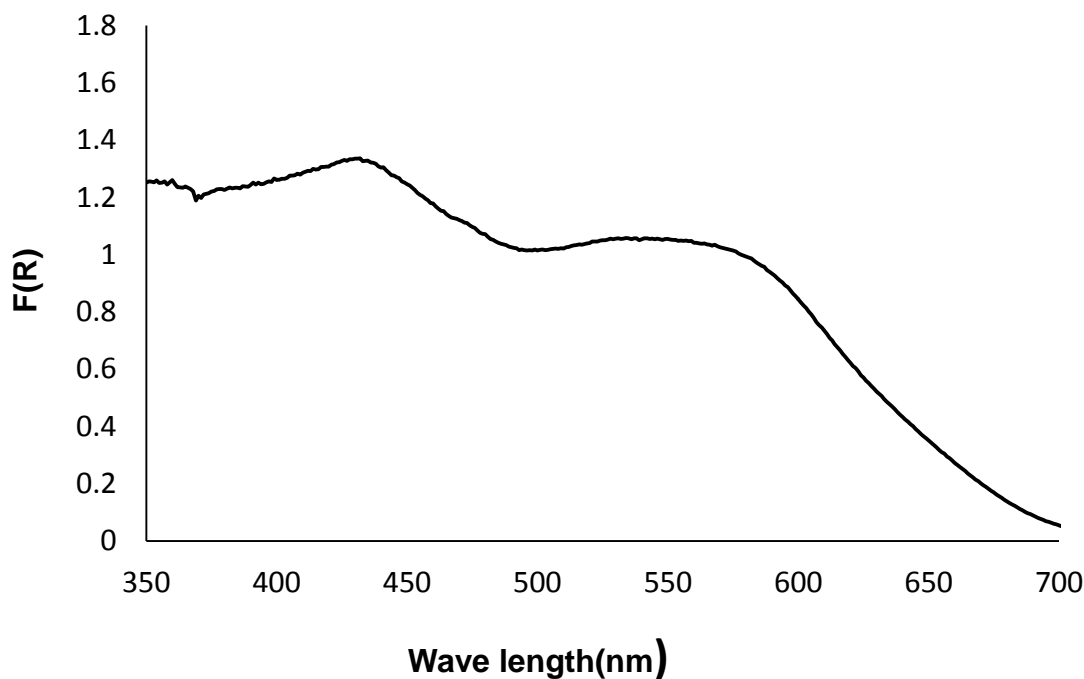
Figure 21. UV-Visible spectra of $[Ru(H_2bpc)Fe(Hbpc)_2(bpc)(H_2O)_2]\cdot6H_2O$ (**2**)

Figure 21 shows UV-vis absorption spectra of compound **2**. The UV-Vis spectra results indicates the electronic properties of the synthesized compound. Compound **2** shown the characteristic absorption band of $[Ru(H_2bpc)_3]^{+2}$ at 434 nm in the visible region. This band can be attributed to the metal-to-ligand charge transfer(MLCT) transition in which an electron is located in ruthenium-based orbitals are promoted into ligand(bpc)-centered π^* orbitals. The λ_{max}(434 nm) of MLCT band of compound **2** shows a red shift in comparision with $[Ru(H_2bpc)_3]^{+2}$ (λ_{max} 427 nm). The UV absorption band of compound **2** shows a blue shift(λ_{max} nm) at 288nm in comparison with $Ru(H_2bpc)_3]^{+2}$, which is corresponds to $\pi-\pi^*$ transition of bpc ligand. These new charge transfer transitions in synthesized compound **2** indicates electronic communication occurred between the ruthenium complex and Fe^{+2} catalyst.

4.2.4 Infrared Spectroscopy

Wave number(cm-1)
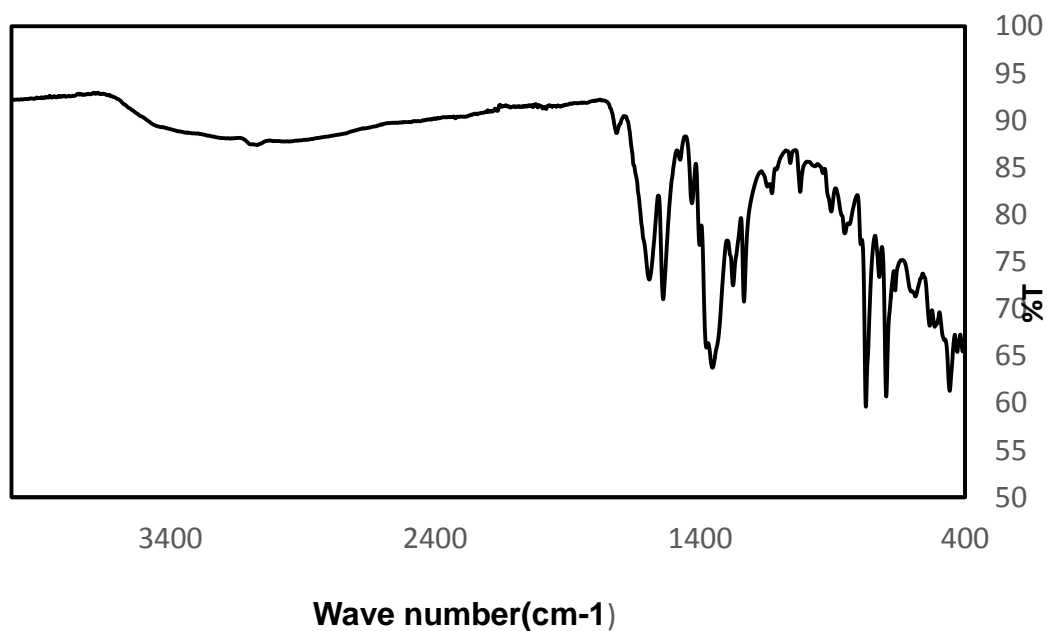
Figure 22. FT-IR spectra of $[Ru(H_2bpc)Fe(Hbpc)_2(bpc)(H_2O)_2]\cdot 6H_2O$ (**2**)

The FT-IR spectra of compound **2** (Figure 22) shows major stretching vibration bands.The vibration band around 3250 cm^{-1} which is the characteristic absorption band of –OH group strecthing vibration of bpc ligand and water molecule. Another absorption band observed around 1721 cm^{-1} which is attributed to the caboxyl group (C=O) of bpc ligand. Several absorption bands located between 1400-1900 cm^{-1} which corresponds to the characteristic stretching vibrations of bpc(2,2'-bypyridine-4,4'- dicarboxylic acid) ligands.

4.2.5 Fluorescence Spectroscopy
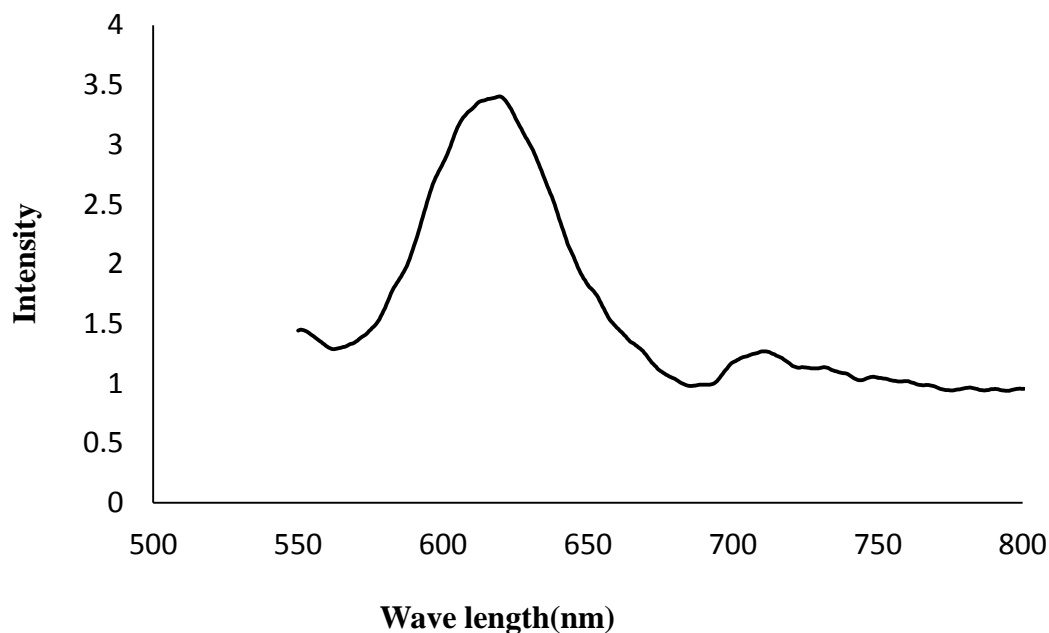
Figure 23. Fluorescence spectra of [Ru(H$_2$bpc)Fe(Hbpc)$_2$(bpc)(H$_2$O)$_2$]·6H$_2$O (**2**)

The fluorescence spectra of compound **2** shown in figure 23. Upon excitation at the λ_{max} (430nm) of the MLCT band of the [Ru(H$_2$bpc)$_3$]$^{+2}$, in compound **2** {[Ru(H$_2$bpc)(Fe(Hbpc)$_2$(bpc)(H$_2$O)$_2$)]·6H$_2$O} showed an emission band at 621 nm, which can be attributed to the emission from the triplet MLCT excited state to the ground state.

The emission of compound **2** exhibits a blue-shift in comparison with that of [Ru(H$_2$bpc)$_3$]$^{+2}$ in aqueous solution (626 nm). These changes may be associated with the strong interactions between ruthenium polypyridyl complex and the Fe^{2+} catalyst.

4.2.6 Thermogravimetric Analysis (TGA)

The thermal behavior of compound **2** was investigated on powder samples under N$_2$ atmosphere in the temparature range between 40°C-700°C. The TG graph of compound **2** exhibited two steps of weight loss. The first weight loss was 11.3% in the temparature range from 40°C -200°C , which is attributed to the loss of water molecules(calcd 11.1%). The weight loss of 64.5% from 250°C to 600°C is corresponding to the decomposition of bpc ligand molecules(calcd 73.0%). After that heating above 720^{0}C no structural changes was observed which indicates compound **2** is stable at high temparature .
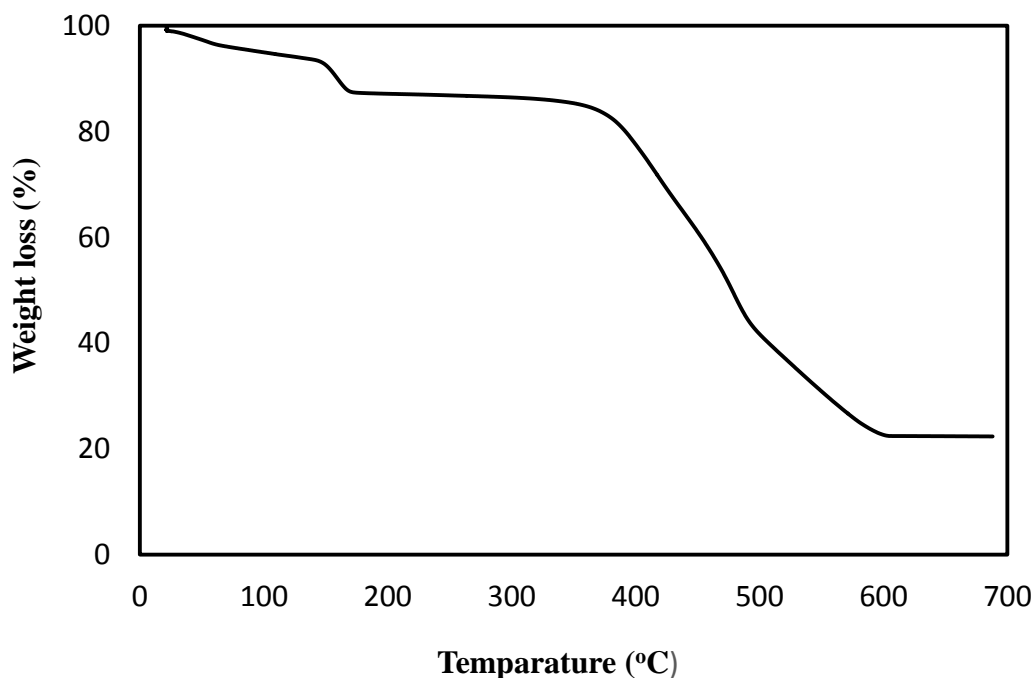
Figure 24. TG plot of TGA analysis of [Ru(H$_2$bpc)Fe(Hbpc)$_2$(bpc)(H$_2$O)$_2$]·6H$_2$O (**2**)

4.3 Conclusion

In summary, using ruthenium polypyridyl complexes as building units and Fe^{+2} metal ion as linkers, we have successfully synthesized $[Ru(H_2bpc)Fe(Hbpc)_2(bpc)(H_2O)_2] \cdot 6H_2O$(**2**) from $RuCl_3.H_2O$, $FeCl_2.4H_2O$ and bpc (2,2'-bipyridine-4,4'-dicarboxylic acid) in presence of solvents such as water, ethanol and 0.5M KOH. The crystal structures of compound **2** was investigated by single X-ray diffraction techniques. X-ray analysis data reveals that the compound **2** possess triclinic crystal system with $P\bar{1}$ space group. The Ru(II) complex ions are bridged by $[Fe(Hbpc)(H_2O)_2]^+$ ions into a one-dimensional (1D) zigzag chain running along the a direction and contains two different metal centers(Ru^{+2}, Fe^{+2}). The ruthenium(Ru^{+2}) metal centers show broad absorption band around 434 nm, due to the MLCT and emission band around 621nm due to the emission of MLCT triplet to singlet state. The 11.1% weight loss was observed upon heating from 40°C -200°C and 73% weight loss from 230-720^{0}C due to evaporation of moisture and decomposition of ligand.

CHAPTER 5

Synthesis and Characterization of [Ru(H₂bpc)(Ni(Hbpc)₂(bpc)(H₂O)₂)]·6H₂O (3)

5.1 Synthesis of [Ru(H₂bpc)(Ni(Hbpc)₂(bpc)(H₂O)₂)]·6H₂O (3)

The synthetic reactions were done under hydrothermal conditions by using 3"×4" Teflon bags placed in 45 ml Teflon-lined stainless steel autoclave reactors. The title compound **3** was prepared by heating a mixture of $RuCl_3 \cdot H_2O$ (0.0068 g, 0.031 mmol), $Ni(NO_3)_2 \cdot 6H_2O$ (0.0124 g, 0.0421 mmol), 2,2'-bypyridine-4,4'-dicarboxylic acid (0.0262 g, 0.107 mmol), 0.35 mL of 0.5 M KOH, 0.5 mL ethanol and 1.0 mL deionized water at 160°C for 72 hours. After cooling to room temperature, orange red crystals of compound **3** were separated from the resulting product by filtration, washed with distilled water and dried in air (61% yield based on H₂bpc).
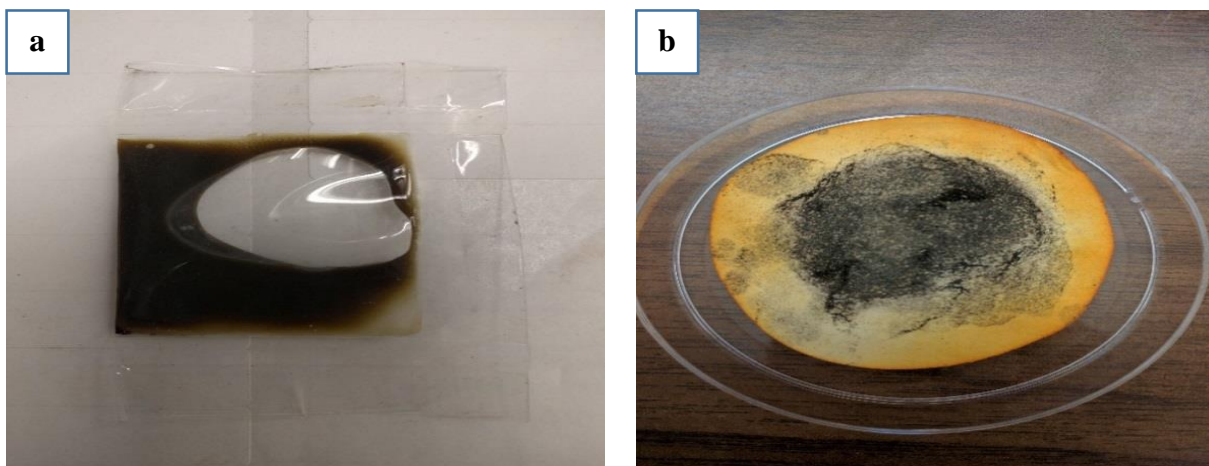
Figure 25. Before(**a**) & After(**b**) heating images of [Ru(H₂bpc)(Ni(Hbpc)₂(bpc)(H₂O)₂)]·6H₂O (**3**)

5.2 Results & Discussions

5.2.1 Synthesis of [Ru(H₂bpc)(Ni(Hbpc)₂(bpc)(H₂O)₂)]·6H₂O (3)

For the making of pure crystals for compound **3**, the following parameters has been changed during the synthesis.

Table 9. Changing of reaction parameters for the synthesis of $[Ru(H_2bpc)(Ni(Hbpc)_2(bpc)(H_2O)_2)]\cdot 6H_2O$ (**3**)

Solvents	Temp	Time	Results
H_2O-1ml, CH_3OH-0.5 ml &KOH-0.35ml	130&160°C	48 & 72 hrs	Impure crystals
H_2O-3ml, CH_3OH-0.5 ml &KOH-0.35ml	130&160°C	48 & 72 hrs	Impure crystals
H_2O-1ml ,CH_3OH-1 ml &KOH-0.4ml	130&160°C	48 &72 hrs	Impure crystals
H_2O-1ml , CH_3OH-1ml &KOH-0.45ml	130&160°C	48 &72 hrs	Impure crystals
H_2O-1ml,C_2H_5OH- 0.5 ml & KOH-3.5 ml	130&160°C	48 hrs	Impure crystals
H_2O-1ml & C_2H_5OH-0.5ml&KOH-0.35ml	**160°C**	**72 hrs**	**pure crystals**
H_2O-3ml & C_2H_5OH-0.5 ml &KOH-0.35ml	130&160°C	72 hrs	Impure crystals
H_2O-1ml & C_2H_5OH-1ml &KOH-0.35ml	160°C	72hrs	Impure crystals
H_2O-1ml & C_2H_5OH-0.5 ml &KOH-0.35ml	180°C	48 & 72 hrs	Impure crystals

5.2.2 Crystal structure of $[Ru(H_2bpc)(Ni(Hbpc)_2(bpc)(H_2O)_2)]\cdot 6H_2O$ (3)

Table 10. Crystal data and structure refinements for [Ru(H$_2$bpc)(Ni(Hbpc)$_2$(bpc)(H$_2$O)$_2$)]·
6H$_2$O (**3**)

Empirical formula	C$_{48}$H$_{44}$N$_8$NiO$_{24}$Ru
Formula weight	1276.67
Temperature	295(2) K
Wavelength	0.71073 Å
Crystal system	Triclinic
Space group	P-1
Unit cell dimensions	a = 11.791(5) Å a= 99.40(3)°.
	b = 15.106(6) Å b= 110.85(2)°.
	c = 16.067(6) Å g = 90.87(3)°.
Volume	2630.1(18) Å^3
Z	2
Density (calculated)	1.546 Mg/m^3
Absorption coefficient	0.734 mm^{-1}
F(000)	1232
Crystal size	0.16 x 0.10 x 0.02 mm^3
Theta range for data collection	1.37 to 27.50°.
Index ranges	-15<=h<=15, -19<=k<=19, -20<=l<=20
Reflections collected	44588
Independent reflections	11931 [R(int) = 0.0454]
Completeness to theta = 27.50°	98.9 %
Max. and min. transmission	0.9855 and 0.8916
Refinement method	Full-matrix least-squares on F^2
Data / restraints / parameters	11931 / 0 / 752
Goodness-of-fit on F^2	1.019
Final R indices [I>2sigma(I)]	R$_1$ = 0.0487, wR$_2$ = 0.1404
R indices (all data)	R$_1$ = 0.0641, wR$_2$ = 0.1507
Largest diff. peak and hole	1.509 and -0.727 e.Å

Table 11. Selected Bond lengths and Bond angles of

[Ru(H$_2$bpc)(Ni(Hbpc)$_2$(bpc)(H$_2$O)$_2$)]·6H$_2$O (**2**)

Bond lengths[Å]		Bond angles [°]	
Ru(1)-N(1)	2.058(3)	N(1)-Ru(1)-N(4)	92.06(13)
Ru(1)-N(4)	2.055(3)	N(1)-Ru(1)-N(6)#1	171.12(12)
Ru(1)-N(6)#1	2.052(3)	N(4)-Ru(1)-N(6)#1	94.94(12)
Ru(1)-N(5)#1	2.063(3)	N(1)-Ru(1)-N(5)#1	95.00(12)
Ru(1)-N(2)	2.070(3)	N(4)-Ru(1)-N(5)#1	171.31(11)
Ru(1)-N(3)	2.075(3)	N(6)#1-Ru(1)-N(5)#1	78.56(12)
Ni(1)-O(6)	2.029(3)	N(5)#1-Ru(1)-N(2)	87.00(12)
Ni(1)-N(7)	2.049(3)	N(1)-Ru(1)-N(3)	100.37(13)
Ni(1)-O(12)	2.047(3)	N(4)-Ru(1)-N(3)	78.94(12)
Ni(1)-N(8)	2.048(3)	N(4)-Ru(1)-N(2)	99.39(12)
Ni(1)-O(2W)	2.079(3)	N(6)#1-Ru(1)-N(2)	94.89(12)
Ni(1)-O(1W)	2.196(3)	N(6)#1-Ru(1)-N(3)	86.37(12)
O(1)-C(11)	1.297(7)	N(5)#1-Ru(1)-N(3)	94.78(12)
O(1)-H(4O)	0.8200	N(2)-Ru(1)-N(3)	178.00(12)
O(2)-C(11)	1.198(7)	O(6)-Ni(1)-N(7)	97.13(13)
O(3)-C(12)	1.196(5)	O(6)-Ni(1)-O(12)	89.17(12)
O(4)-C(12)	1.308(5)	N(7)-Ni(1)-O(12)	173.70(12)
O(4)-H(3O)	0.8200	O(6)-Ni(1)-N(8)	176.28(12)
O(5)-C(23)	1.246(5)	N(7)-Ni(1)-N(8)	79.18(13)
O(6)-C(23)	1.248(5)	O(12)-Ni(1)-N(8)	94.52(12)
O(7)-C(24)	1.221(6)	O(6)-Ni(1)-O(2W)	86.92(12)
O(8)-C(24)	1.289(5)	N(7)-Ni(1)-O(2W)	91.41(14)
O(9)-C(35)	1.220(5)	O(12)-Ni(1)-O(2W)	88.76(13)
O(10)-C(35)	1.267(5)	N(8)-Ni(1)-O(2W)	92.72(13)
N(5)-Ru(1)#2	2.063(3)	O(6)-Ni(1)-O(1W)	91.19(11)
N(6)-Ru(1)#2	2.052(3)	N(7)-Ni(1)-O(1W)	87.27(13)
N(1)-C(1)	1.334(5)	O(12)-Ni(1)-O(1W)	92.79(11)
N(1)-C(5)	1.371(5)	N(8)-Ni(1)-O(1W)	89.06(12)

Symmetry transformations used to generate equivalent atoms:

#1 x-1,y,z   #2 x+1,y,z
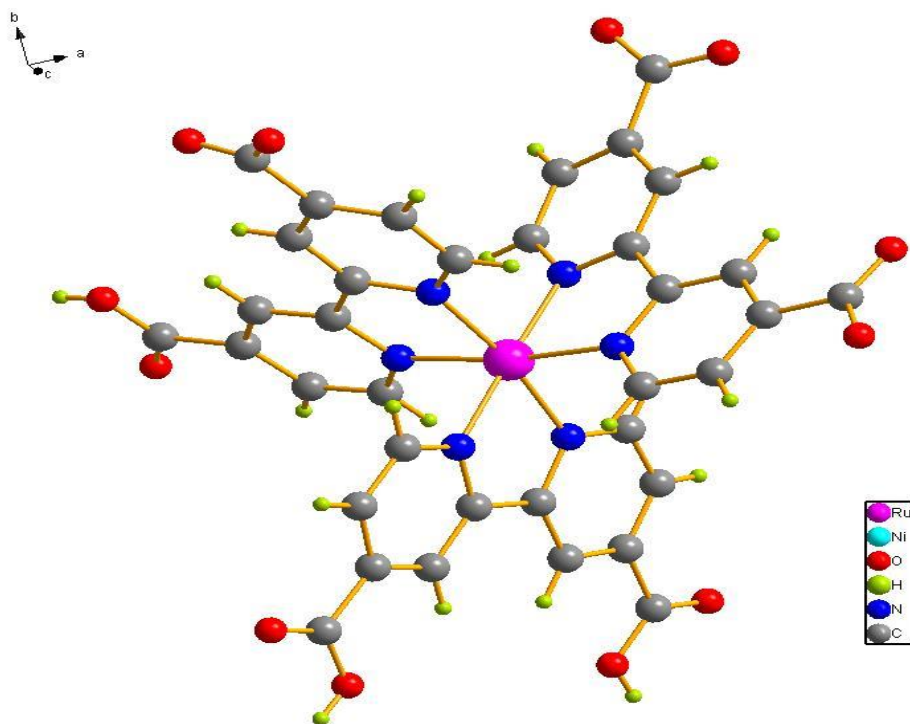
Figure 26. Geometry of [Ru(H$_2$bpc)(Hbpc)(bpc)] in

[Ru(H$_2$bpc)(Ni(Hbpc)$_2$(bpc)(H$_2$O)$_2$)]·6H$_2$O (**3**)
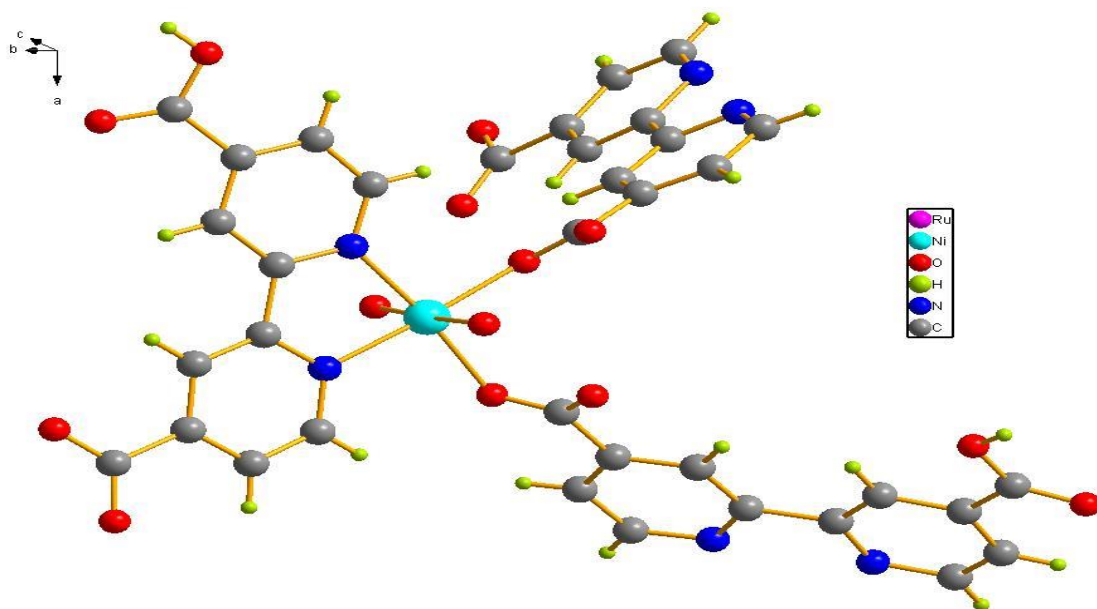
Figure 27. Geometry of [Ni(Hbpc)$_2$(bpc)(H$_2$O)$_2$] in

[Ru(H$_2$bpc)(Ni(Hbpc)$_2$(bpc)(H$_2$O)$_2$)]·6H$_2$O (**3**)
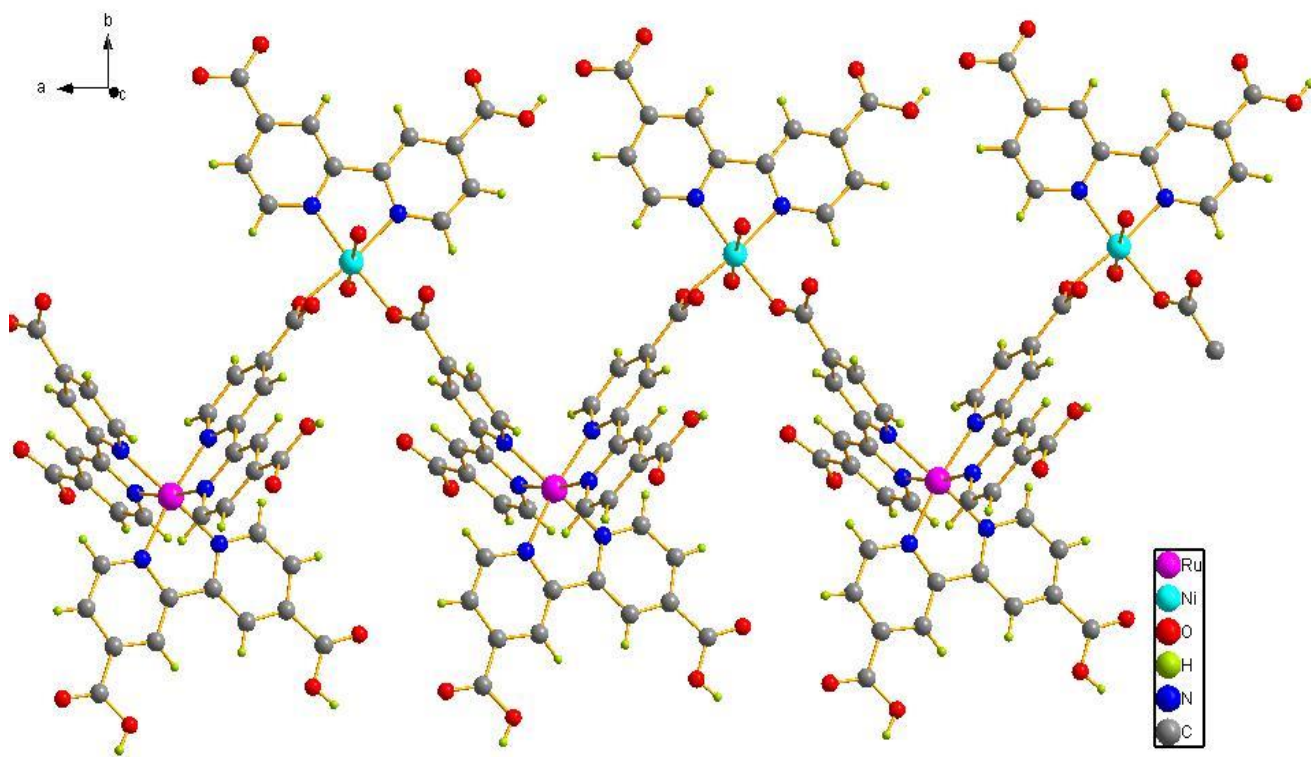
Figure 28. One-dimensional structure of $[Ru(H_2bpc)(Ni(Hbpc)_2(bpc)(H_2O)_2)]\cdot 6H_2O$ (**3**)

Single crystal X-ray data was collected on on a Nonius kappa CCD diffractometer equipped with graphite monochromated Mo Kα radiation with a radiation wavelength of 0.71073Å.   The data reveals that compound 3 or $\{[Ru(H_2bpc)(Fe(Hbpc)_2(bpc)(2H_2O))]\}$ possess triclinic crystal system with the space group $P\overline{1}$. The asymmetric unit contains one Ru(II), one Ni(II) ion, two Hbpc$^-$ ligand anions, one bpc^{2-} ion, one H$_2$bpc ligand molecule, two coordinated water and several lattice water molecules. Each chiral ruthenium(II) center bonds to three organic ligands through Ru-N bonds to form an octahedral coordination geometry $[Ru(H_2bpc)(Hbpc)(bpc)]^-$(Fig 26). The Ru-N bond lengths are in the range of 2.058(3)-2.075(2) Å. The Ru(II) complex ions are coordinated by $[Ni(Hbpc)_2(bpc)(H_2O)_2]$ $^-$ ions into a one-dimensional (1D) zigzag chain running along the *a* direction (Fig 28). The

Ni(II) ions in the 1D chain adopt a octahedral geometry $[Ni(Hbpc)(bpc)_2(H_2O)]^-$ with two oxygen atoms from two carboxylate groups, two oxygen atoms from two water molecules and two nitrogen atoms of a Hbpc ligand(fig 27). The one Ni-O bond length involving water molecules in the apical position is much longer 2.196(3)Å than those involving another water molecule 2.079(3)Å and carboxylate oxygens (2.029(3) and 2.048(2)Å). The Ni-N bond lengths are in the normal range (2.000(3) and 2.014(3)Å). The coordinate water molecules can be potentially removed to give a MOF with open coordination sites, which are considered as key factors in the application of MOFs. It is interesting to note that there are three forms of the H_2bpc ligand molecule in the compound: H_2bpc, $Hbpc^-$ and bpc^{2-}. This can be confirmed by the charge balance of the counter ions in the chemical formula and IR spectroscopy of the solid (Fig 30).

5.2.3 UV-Visible Spectroscopy
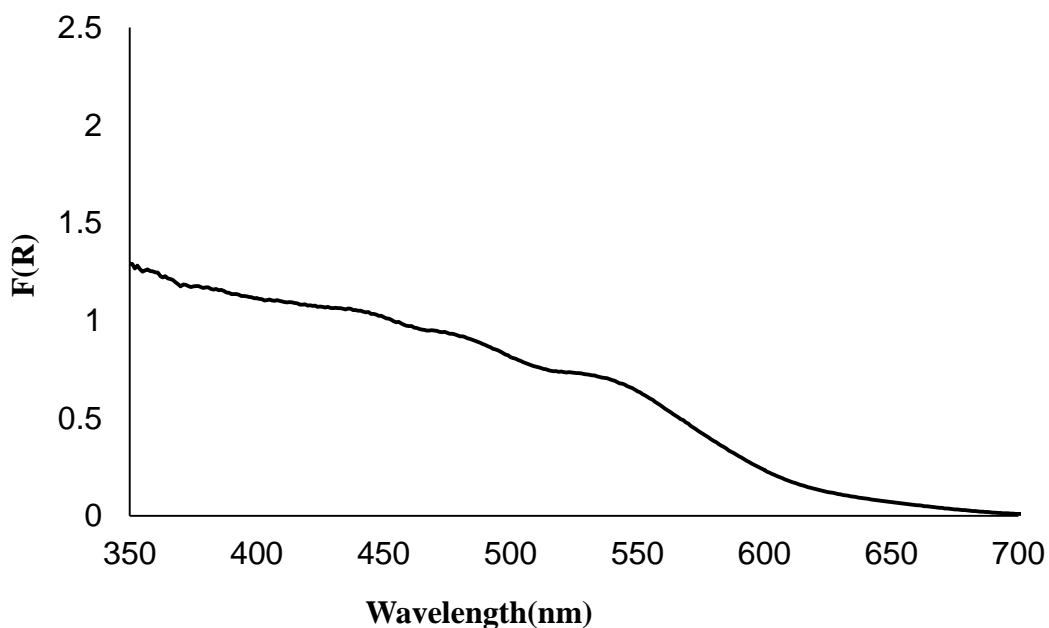
Figure 29. UV-visible spectra of $[Ru(H_2bpc)(Ni(Hbpc)_2(bpc)(H_2O)_2)]\cdot6H_2O$ (**3**)

Figure 29 displays UV-vis absorption spectra of compound **3**. The UV-vis spectra results indicates the electronic properties of the synthesized compound. Compound **3** shown the characteristic absorption band of $[Ru(H_2bpc)_3]^{+2}$ at 435nm in the visible region. This band can be attributed to the metal-to-ligand charge transfer(MLCT) transition in which an electron is located in ruthenium-based orbitals are promoted into ligand(bpc)-centered π^* orbitals. This absorption band shifted to red compared to the discrete $[Ru(H_2bpc)_3]^{+2}$, which shows a broad band at 427nm.

The UV-absorption band was located at 287 nm corresponds to a ligand centered π-π^*transition of bpc (2,2'-bipyridine-4,4'-dicarboxylate) ligand which is overlapped by MLCT absorption band. These changes of charge transitions in compound-1 clearly indicates that the electronic communication occurred between ruthenium polypyridyl complex and nickle (Ni^{2+}) complex

5.2.4 Infrared Spectroscopy
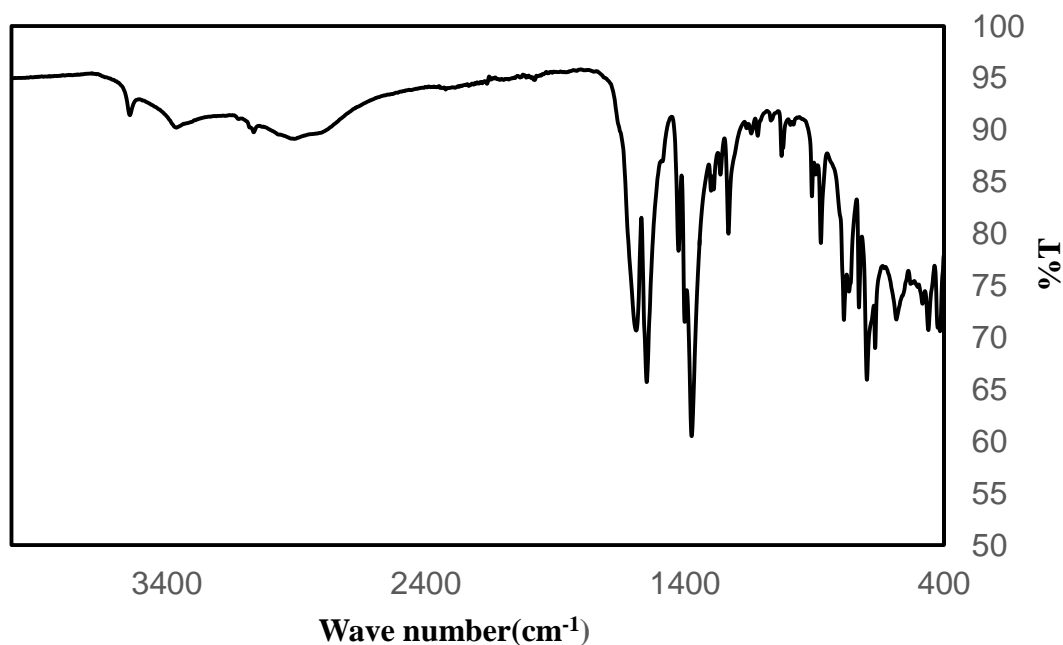
Figure 30. FTIR spectra of $[Ru(H_2bpc)(Ni(Hbpc)_2(bpc)(H_2O)_2)]\cdot 6H_2O$ (**3**)

The FTIR spectra results shown major stretching vibration bands in compound **3**. The vibration band around 3356 cm^{-1} which is the characteristic absorption band of –OH group strecthing vibration of bpc ligand and water molecule. Another absorption band observed around 1589 cm^{-1} which is attributed to the caboxyl group (C=O) of bpc ligand. Several absorption bands located between 1400-1900 cm^{-1} which corresponds to the characteristic stretching vibrations of bpc(2,2'-bypyridine-4,4'-dicarboxylic acid) ligands.

5.2.5 Fluorescence Spectroscopy
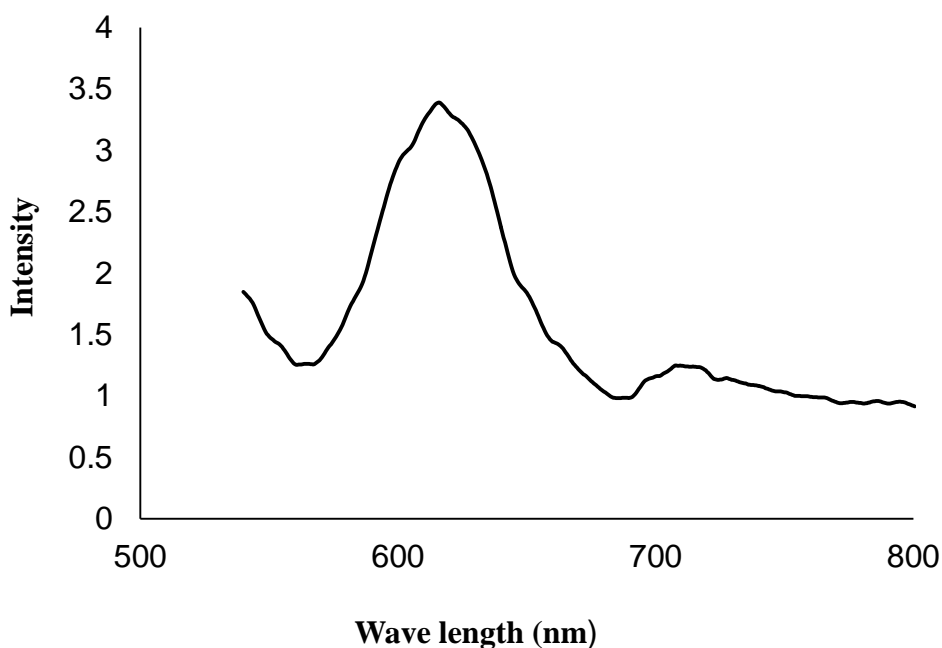
Figure 31. Fluorescence spectra of compound 3

Upon excitation at the λ_{max} (440 nm) of the MLCT band of the ruthenium polypyridyl complex, an emission centered band was observed at 626 nm. For compound 3 an emission band was observed with lower intensity around 601-606 nm upon excitation at λ_{max} (450nm) due to the coordination of copper catalyst with ruthenium polypyridyl complex.

The emission bands for both compounds can be attributed to the emission of energy from triplet MLCT excited state ruthenium to the singlet ground state.

5.2.6 Thermogravimetric Analysis (TGA)
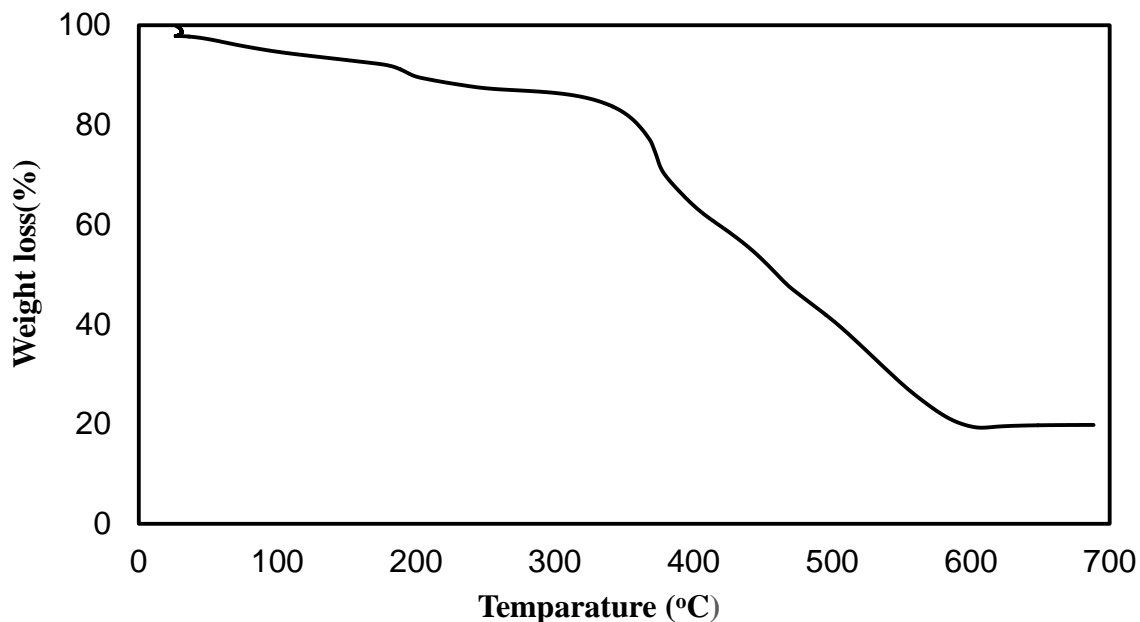
Figure 32. Thermogravimetric analysis of $[Ru(H_2bpc)(Ni(Hbpc)_2(bpc)(H_2O)_2)]\cdot 6H_2O$ (**3**)

The thermal behavior of compound **3** was investigated on powder samples under N_2 atmosphere in the temparature range between 24°C-700°C. The TG graph of compound **3** exhibited two steps of weight loss. The first weight loss was 10.7 % in the temparature range from 40°C -200°C , which is attributed to the loss of water molecules. The weight loss from 250°C to 600°C is corresponding to the decomposition of bpc ligand molecules.

5.3 Conclusion

In summary, we have successfully synthesized a new compound $[Ru(H_2bpc)(Ni(Hbpc)_2(bpc)(H_2O)_2)]\cdot6H_2O$ (**3**) from $RuCl_3.H_2O$, $Ni(NO_3)_2.6H_2O$ and bpc in a mixture of solvents such as water and ethanol. The crystal of compound **3** possess triclinic crystal system with $P\overline{1}$ space group. The Ru(II) complex ions are coordinated by $[Ni(Hbpc)_2(bpc)(H_2O)_2]^-$ ions into a one-dimensional (1D) zigzag chain running along the *a* direction. The ruthenium(Ru^{+2}) metal centers show broad absorption band around 435 nm, due to the MLCT and emission band around 626 nm due to the emission of MLCT triplet to singlet state. Upon heating, the weight loss was observed in compound **3** at two different temparatures because of the evoparation of water molecules and decomposition of organic ligand in compound **3**.

CHAPTER 6

Conclusion

The synthesis and characterization of metal-organic frameworks have been attracting great attention as efficient photocatalysts by the researchers, due to their high affinity, chemical and structural tunability and broad UV-visible absorption bands. Taking advantage of broad absorption of MLCT or ligand π- π* bands, many photocatalytic MOFs have been reported.[36] In addition to absorption, the charge separation between metal ions and ligands is the second advantage of MOFs as photocatalysts.

Ruthenium polypyridyl complexes have been extensively used as excellent photosensitizers in many research areas, due to their unique properties such as broad absorption bands in the visible region, redox properties, long-lived lifetime of excited states. However, the major drawback of these complexes is that it is very difficult to optimize both light absorption and catalytic activity at a single solid. To overcome the drawback, researchers are trying to investigate new MOFs by the incorporation of ruthenium polypyridyl complexes into the solid materials.

With this aspect, we have successfully synthesized three new MOFs containing ruthenium polypyridine complexes $[Ru(H_2bpc)_3]^{2+}$ with metal ions (Cu^{2+}, Fe^{2+}, or Ni^{2+}). In this thesis, the synthesis and structures of three new MOFs have been described. Our experimental results demonstrate that the self-assembled hybrid solid of luminescent $\{[Ru(II)/Cu(II)],[Ru(II)/Fe(II)]$ & $Ru(II)/Ni(II)\}$ polypyridyl metal-organic frameworks can be carried out by the hydrothermal method/solvothermal method.

Compound **1** ($[Ru(H_2bpc)(Cu(bpc)(Hbpc)_2(H_2O))]\cdot5.5H_2O$) crystallizes in the triclinic space group $P\bar{1}$. The asymmetric unit consist one Ru(II),one Cu(II) ion, one bpc^{2-} ion, two

63

Hbpc$^-$ ligand anions ,one H$_2$bpc molecule and one water molecule. The Ru-N bond lengths are in the range of 2.046(2)-2.078(2) Å. The Ru(II) complex ions are bridged by [Cu(bpc)(Hbpc)$_2$(H$_2$O)]$^+$ ions into a one-dimensional (1D) zigzag chain running along the *a* direction and the Cu-O bond length (2.248(3)Å) involving water is much longer than those involving carboxylate oxygens (1.938(2) and 1.949(2)Å). Compound **2** ([Ru(H$_2$bpc)(Fe(bpc)(Hbpc)$_2$(H$_2$O)$_2$]·6H$_2$O) has same crystal structure as compound 1. An interesting feature of compound **2** is that the Fe^{2+} ion is coordinated with two water molecules. The two Fe-O bond lengths involving water have similar lengths (2.094Å & 2.048 Å). Compound **3**, ([Ru(H$_2$bpc)(Ni(bpc)(Hbpc)$_2$(H$_2$O)$_2$]·6H$_2$O), is very similar to compound **2**, but one Ni-O bond length involving water molecules in the apical position is much longer (2.196(3)Å) than those involving second water molecule (2.079(3)Å) and carboxylate oxygens (2.029(3) and 2.048(2)Å).

All new MOFs exhibit the broad characteristic UV-Visible absorption band of [Ru(H$_2$bpc))$_3$)]$^{2+}$. These bands are attributed to the metal-to-ligand charge transfer (MLCT) transition, in which transition of electrons from metal based *d*-orbitals to ligand based π* orbitals. These compounds have luminescence under visible light. Compound **1** emits around 610nm, upon excitation at the λ$_{max}$ (440 &480nm). Compound **2** emits at 621nm ; compound **3** emits at 626nm upon exications at 450& 460 nm. All these emission bands are attributed to the emission of energy from triplet MLCT excited state to the singlet ground state. These spectroscopic studies clearly indicate that strong electronic communication occurred in the synthesized MOFs.

Thermogravimetric analysis(TGA) results of all these three compounds shows that the ligands of these compounds start decomposition at around 200 °C. This means these MOFs

are stable under normal temparature. Studies are underway to investigate the photocatalytic properties of these three new MOF materials.

In the future, we expect that the ligand modification will allow the synthesis of new solid materials containing ruthenium polypyridine complexes coordinated to catalysts through coordinated bonds and these new materials with enhanced photochemical properties.

REFERENCES

1. Barber, J.; Tran, P.D, "From natural to artificial photosynthesis", J.R.soc. Interface **2013**, 10, 20120984.

2. Li, K.; Peng, B.; Peng, T, "Recent Advances in Homogeneous Photocatalytic CO2 Conversion to Solar Fuels", ACSCatal. **2016**, 6, 7485– 7527.

3. IPCC, Climate Change 2014-Impacts, Adaptation and Vulnerability: Regional Aspects; Cambridge University Press: **2014**.

4. Earth System Research Laboratory:

   http://www.esrl.noaa.gov/gmd/ccgg/trends/index.html,2012.

5. Petit, J. R.; Jouzel, J.; Raynaud, D.; Barkov, N. I.; Barnola, J. M.; Basile, I.; Bender, M. Chappellaz, J.; Davis, M.; Delaygue, G.; Delmotte, M.; Kotlyakov, V. M.; Legrand, M.;Lipenkov, V. Y.; Lorius, C.; Pepin, L.; Ritz, C.; Saltzman, E.; Stievenard, M, "Climate and atmospheric history of the past 420,000 years from the Vostok ice core, Antarctica", Nature,1999, 399, 429-436.

6. U.S. Energy Information Admistration. International energy statistics.http://www.eia.gov/cfapps/ipdbproject/iedindex3.cfm?tid=2&pid=alltypes &aid=&ci   d=regions&syid=2008&eyid=2011&unit=BKWH (accessed July 7,2015).

7. IPCC, 2007: Climate Change 2007: The Physical Science Basis. Contribution of Working Group I to the Fourth Assessment Report of the Intergovernmental Panel on Climate Change [Solomon, S., D. Qin, M. Manning, Z. Chen, M. Marquis, K.B.

Averyt, M.Tignor and H.L. Miller (eds.)]. Cambridge University Press, Cambridge, United Kingdom and New York, NY, USA.

8. Damyanov, N. N.; Matthews, H. D.; Mysak, L. A, "Observed decreases in the Canadian outdoor skating season due to recent winter warming. Environmental Research Letters", Environ. Res. Letts. **2012**, 7, 014028.

9. Tabassum, A.; Premalatha, M.; Abbasi, T.; Abbasi, S. A., "Renewable and Sustainable Energy Reviews" Rev.**2014,** 31, 270-288.

10. Andersson, I.; Knight, S.; Schneider, G.; Lindqvist, Y.; Lundqvist, T.; Brändén, C.-I.; Lorimer, "Current Research in Photosynthesis", Nature 1989, 337, 229.

11. Yarris, Lynn. "Turning Sunlight into Liquid Fuels: Berkeley Lab Researchers Create a Nano-sized Photocatalyst for Artificial Photosynthesis". Berkeley Lab News Center. Lawrence Berkeley National Laboratory. Retrieved 16 January 2012.

12. Magnuson, Ann; Anderlund, Magnus; Johansson, Olof; Lindblad, Peter; Lomoth, Reiner; Polivka, Tomas; Ott, Sascha; Stensjö, Karin; Styring, Stenbjörn; Sundström, Villy; Hammarström, LeiF, "Biomimetic and Microbial Approaches to Solar Fuel Generation". Accounts of Chemical Research. **42** (12):1899–1909.

13. Parkinson, B. "Advantages of Solar Hydrogen Compared to Direct Carbon Dioxide Reduction for Solar Fuel Production", ACS Energy Lett. 2016, 1, 1057−1059.

14. Xie, S.; Wang, Y.; Zhang, Q.; Deng, W.; Wang, Y, **"**Carbon dioxide-enhanced photosynthesis of methane and hydrogen from carbon dioxide and water over Pt-promoted polyaniline–TiO_2 nanocomposites",ACS Catal. 2014, 4, 3644−3653.

15. Gellman, A. J.; Shukla, N,"Catalysis by Materials with Well-Defined Structures", Nat. Mater, 2009, 8, 87−88.

16. Xu, Y.-F.; Yang, M.-Z.; Chen, B.-X.; Wang, X.-D.; Chen, H.-Y.; Kuang, D.-B.; Su, C.-Y. J. Am, "A CsPbBr3 Perovskite Quantum Dot/Graphene Oxide Composite for Photocatalytic CO2 Reduction", Chem. Soc. 2017, 139, 5660−5663.

17. Li, X.; Wen, J.; Low, J.; Fang, Y.; Yu, J, "The fabrication and photoelectrocatalytic study of composite ZnSe/Au/TiO$_2$ nanotube films", Science China Mater. 2014, 57, 70−100.

18. Tseng, I. H.; Chang, W.-C.; Wu, J. C. S. Appl. Catal., B, 2002, 37, 37−48.

19. Kraeutler, B.; Bard, A. J. J, "Heterogeneous photocatalytic synthesis of methane from acetic acid - new Kolbe reaction pathway", J.Am. Chem. Soc. 1978, 100, 2239− 2240.

20. Yui, T.; Kan, A.; Saitoh, C.; Koike, K.; Ibusuki, T.; Ishitani, O, "Photochemical Reduction of CO$_2$ Using TiO$_2$: Effects of Organic Adsorbates on TiO$_2$ and Deposition of Pd onto TiO$_2$", ACS Appl. Mater. Interfaces 2011, 3, 2594−2600.

21. Inoue, T.; Fujishima, A.; Konishi, S.; Honda, K, **"**Photoelectrocatalytic reduction of carbon dioxide in aqueous suspensions of semiconductor powders",Nature 1979, 277, 637−638.

22. Fujishima and K. Honda,"Electrochemical Photolysis of Water at a Semiconductor Electrode", Nature, 1972, 238, 37–38.

23. X. Chen and A. Selloni, "Introduction: Titanium Dioxide (TiO$_2$) Nanomaterials",Chem. Rev., 2014, 114, 9281–9282.

24. G. Liu, H. G. Yang, J. Pan, Y. Q. Yang, G. Q. Lu and H.-M.Cheng, "Titanium Dioxide Crystals with Tailored Facets",Chem. Rev., 2014, 114, 9559–9612.

25. Kapilashrami, Y. Zhang, Y.-S. Liu, A. Hagfeldt and J. Guo, "Probing the Optical Property and Electronic Structure of TiO_2Nanomaterials for Renewable Energy Applications", Chem. Rev., 2014, 114, 9662–9707.

26. X. Chen, L. Liu, Y. Y. Peter and S. S. Mao, "Increasing solar absorption for photocatalysis with black hydrogenated titanium dioxide nanocrystals", Science, 2011,331, 746–750.

27. S. Linic, P. Christopher and D. B. Ingram, "Plasmonic-metal nanostructures for efficient conversion of solar to chemical energy", Nat. Mater.,2011, 10, 911–921.

28. Iizuka, K.; Wato, T.; Miseki, Y.; Saito, K.; Kudo, "Photocatalytic reduction of carbon dioxide over Ag cocatalyst-loaded ALa4Ti4O15 (A = Ca, Sr, and Ba) using water as a reducing reagent",A. J. Am. Chem. Soc. 2011, 133, 20863−20868.

29. Zhang, J.; Yu, J.; Jaroniec, M.; Gong, J. R, "Noble Metal-Free Reduced Graphene Oxide-$Zn_xCd_{1−x}S$ Nanocomposite with Enhanced Solar Photocatalytic H_2-Production Performance", Nano Lett. 2012, 12, 4584−4589.

30. Liu, Q.; Zhou, Y.; Kou, J.; Chen, X.; Tian, Z.; Gao, J.; Yan, S.; Zou, Z, "High-yield synthesis of ultralong and ultrathin Zn2GeO4 nanoribbons toward improved photocatalytic reduction of CO2 into renewable hydrocarbon fuel", J. Am. Chem. Soc. 2010, 132, 14385−14387.

31. Huang, H.; Lin, J.; Zhu, G.; Weng, Y.; Wang, X.; Fu, X.; Long, J. "Solution-processed two-dimensional MoS2 nanosheets: preparation, hybridization and applications" ,Angew. Chem., Int. Ed. 2016, 55, 8314−8318.

32. Yu, J.; Low, J.; Xiao, W.; Zhou, P.; Jaroniec, M. J, "Enhanced Photocatalytic CO_2-Reduction Activity of Anatase TiO_2 by Coexposed {001} and {101} Facets",Am. Chem. Soc. 2014, 136, 8839−8842

33. Kim, K.; Razzaq, A.; Sorcar, S.; Park, Y.; Grimes, C. A.; In, S.-I. RSC Adv. 2017, 6, 38964−38971.

34. Wang, J.-C.; Zhang, L.; Fang, W.-X.; Ren, J.; Li, Y.-Y.; Yao, H.- C.; Wang, J.-S.; Li, Z.-J, "Indirect Z-Scheme BiOI/g-C3N4 Photocatalysts with Enhanced Photoreduction CO2 Activity under Visible Light Irradiation", ACS Appl. Mater. Interfaces 2015, 7, 8631− 8639.

35. Jin-Liang Wang,† Cheng Wang,† and Wenbin Lin, "Metal−Organic Frameworks for Light Harvesting and Photocatalysis", ACS Catal., **2012**, 2 (12), pp 2630–2640.

36. M. A. Nasalevich, M. G. Goesten, T. J. Savenije, F. Kapteijn and J. Gascon, "Metal–organic frameworks as heterogeneous photocatalysts: advantages and challenges", Chem. Commun., 2013, **49**, 10575–10577.

37. C. Gomes Silva, I. Luz, F. X. Llabrés i Xamena, A. Corma and H. García, "Water stable Zr-benzenedicarboxylate metal-organic frameworks as photocatalysts for hydrogen generation",
Chem. – Eur. J., 2010, **16**, 11133–11138.

38. A. Fateeva, P. A. Chater, C. P. Ireland, A. A. Tahir, Y. Z. Khimyak, P. V. Wiper, J. R. Darwent and M. J. Rosseinsky, **"**A water-stable porphyrin-based metal-organic framework active for visible-light photocatalysis"**,** Angew. Chem., Int. Ed., 2012, **51**, 7440–7444.

39. P. Wu, C. He, J. Wang, X. Peng, X. Li, Y. An and C. Duan, "Photoactive chiral metal-organic frameworks for light-driven asymmetric α-alkylation of aldehydes**,**J. Am. Chem. Soc., 2012, **134**, 14991–14999.

40. X. Zhang, M. A. Ballem, Z.-J. Hu, P. Bergman and K. Uvdal, "Nanoscale Light-Harvesting Metal-Organic Frameworks", Angew. Chem., Int. Ed., 2011, **50**, 5729–5733.

41. X. Zhang, Z.-K. Chen and K. P. Loh, "Coordination-Assisted Assembly of 1-D Nanostructured Light-Harvesting Antenna", J. Am. Chem. Soc., 2009, **131**, 7210–7211.

42. S. Jin, H.-J. Son, O. K. Farha, G. P. Wiederrecht and J. T. Hupp, "Energy transfer from quantum dots to metal-organic frameworks for enhanced light harvesting**,** J. Am. Chem. Soc., 2013, **135**, 955–958.

43. C. A. Kent, B. P. Mehl, L. Ma, J. M. Papanikolas, T. J. Meyer and W. Lin, "Energy transfer dynamics in metal-organic frameworks",J. Am. Chem. Soc., 2010, **132**, 12767–12769.

44. A. R. Ramya, D. Sharma, S. Natarajan and M. L. P. Reddy, "Highly Luminescent and Thermally Stable Lanthanide Coordination Polymers Designed from 4-(Dipyridin-2-yl)aminobenzoate: Efficient Energy Transfer from Tb^{3+} to Eu^{3+} in a Mixed Lanthanide Coordination Compound"

Inorg. Chem., 2012, **51**, 8818–8826.

45. J. H. Cavka, S. Jakobsen, U. Olsbye, N. Guillou, C. Lamberti, S. Bordiga and K. P. Lillerud, "A new zirconium inorganic building brick forming metal organic frameworks with exceptional stability" J. Am. Chem. Soc., 2008, **130**, 13850–13851.

46. Y. Fu, D. Sun, Y. Chen, R. Huang, Z. Ding, X. Fu and Z. Li, "An amine-functionalized titanium metal-organic framework photocatalyst with visible-light-induced activity for CO2 reduction",Angew. Chem., Int. Ed., 2012, **51**, 3364–3367.

47. Teng Zhang and Wenbin Lin * "Metal-Organic frameworks for artificial photosynthesis and photocatalyssi"(Review Article) Chem. Soc. Rev., 2014, **43**, 5982-5993.

48. Narayanam, J. M. R.; Stephenson, C. R, "Visible light photoredox catalysis: Applications in organic synthesis", J. Chem. Soc. Rev. 2011, 40, 102−113.

49. a) Van Houten, J.; Watts. R. J, "Photochemistry of tris(2,2'-bipyridyl)ruthenium(II) in aqueous solutions",Inorg. Chem. 1978, 17(12), 3381-3385.

    (b) Seery, M. K.; Guerin, L.; Forster, R. J.; Gicquel, E.; Hultgren, V.; Bond, A. M.; Wedd, A. G.; Keyes, T. E. J. Phys. Chem. A. 2004, 108, 7399-7405.

50. (a) Meyer, T. J, "Photochemistry of metal coordination complexes: metal to ligand charge transfer excited states",Pure & Appl. Chem. 1986, 58(9), 1193-1206. 67.

     (b) Damrauer, N. H.; Cerullo, G.; Yeh, A.; Boussie, T. R.; Shank, C. V.; McCusher, J. K",Femtosecond Dynamics of excited –state Evolution" ,Science. 1997, 275, 54-57. (c) Mori, K.; Kawashima, M.; Che, M.; Yanmashita, H. Angew. Chem. Int. Ed. 2010, 49, 1-5.

51. (a) Tamaki, Y.; Morimoto, T.; Koike, K.; Ishitani, "Photocatalytic CO_2 reduction with high turnover frequency and selectivity of formic acid formation using Ru(II) multinuclear complexes", O. Proc. Natl. Acad. Sci. U. S. A. 2012, 109, 15673−15678.

(b) Kuramochi, Y.; Kamiya, M.; Ishida, H, "Photocatalytic CO2 reduction in N,N-dimethylacetamide/water as an alternative solvent system",Inorg. Chem. 2014, 53, 3326.

52. Juris, A.; Campagna, S.; Balzani, V.; Gremaud, G.; Zelewsky, A. V. Inorg. Chem. 1988, 27(20), 3652-3655.

53. (a) Desilvestro, J.; Graetzel, M.; Kavan, L.; Moser, J.; Augustynski, "Highly efficient sensitization of titanium dioxide", J. J. Am. Chem. Soc. 1985, 107(10), 2988-2990.

(b) Vlachopoulos, N.; Liska, P.; Augustynski, J.; Graetzel, M. J. Am. Chem. Soc. 1988, 110(4), 1216-1220.

54. (a) Durham, B.; Walsh, J. L.; Carter, C. L.; Meyer, T. J. "Synthetic applications of photo substitution reactions of poly(pyridyl) complexes of ruthenium(II)" Inorg. Chem. 1980, 19, 860-865.

(b) Wu, Q.; Wang, L. Synthesis. 2008, 13, 2007-2012.

55. Wight, A. P.; Davis, M. E. "Design and Preparation of Organic−Inorganic Hybrid Catalysts", Chem. Rev. 2002, 102, 3589-3614.

56. Yusuke Tamaki and Osamu Ishitani, "Supramolecular photocatalysts constructed with a photosensitizer unit with two tridentate ligands for CO2 reduction" Faraday Discussions 2017, 198, 319.

57. B. Gholamkhass, H. Mametsuka, K. Koike, T. Tanabe, M. Furue, O. Ishitani, "New and futuredevelopments in catalysis:Solar photocatalysis" Inorg. Chem. 44 (2005) 2326.

58. Bobak Gholamkhass,† Hiroaki Mametsuka,‡ Kazuhide Koike,§ Toyoaki Tanabe,| Masaoki Furue,| and Osamu Ishitani*, "Architecture of Supramolecular Metal Complexes for Photocatalytic CO_2 Reduction: Ruthenium−Rhenium Bi- and Tetranuclear Complexes", Inorg. Chem. 2005, 44, 2326−2336.

59. Z.Y. Bian, K. Sumi, M. Furue, S. Sato, K. Koike, O. Ishitani, "Conjugation effect of the bridging ligand on the CO_2 reduction properties in difunctional photocatalysts",Dalton Trans. 47 (2008) 10801.

60. (a) Narayanam, J. M. R.; Stephenson, C. R. J. Chem. Soc. Rev. 2011, 40, 102−113.

(b) Yui, T.; Tamaki, Y.; Sekizawa, K.; Ishitani, O. Top. Curr. Chem. 2011, 303, 151−184.

61. Zhang, S.; Han, L.; Li, L.; Cheng, J.; Yuan, D.; Luo, J., "A Highly Symmetric Metal–Organic Framework Based on a Propeller-Like Ru-Organic Metalloligand for Photocatalysis and Explosives Detection", Crystal Growth & Design 2013, 13 (12), 5466-5472.

62. Ma, S.; Sun, D.; Ambrogio, M.; Fillinger, J. A.; Parkin, S.; Zhou, H, "Framework-Catenation Isomerism in Metal−Organic Frameworks and Its Impact on Hydrogen Uptake", J. Am. Chem. Soc. 2007, 129, 1858−1859.

63. Dinca, M.;˘ Dailly, A.; Tsay, C.; Long, J. R, "Expanded Sodalite-Type Metal−Organic Frameworks: Increased Stability and H$_2$ Adsorption through Ligand-Directed Catenation",

Inorg. Chem. 2008, 47, 11−13.

64. Bureekaew, S.; Sato, H.; Matsuda, R.; Kubota, Y.; Hirose, R.; Kim, J.; Kato, K.; Takata, M.; Kitagawa, S. Angew. Chem., Int. Ed. 2010, 49, 7660−7664.

65. Zhang, S.; Li, L.; Zhao, S.; Sun, Z.; Luo, J., "Construction of Interpenetrated Ruthenium Metal–Organic Frameworks as Stable Photocatalysts for CO2 Reduction".Inorganic Chemistry 2015, 54 (17), 8375-8379.

66. Kobayashi, A.; Ohba, T.; Saitoh, E.; Suzuki, Y.; Noro, S.-i.; Chang, H.-C.; Kato, M., "Flexible Coordination Polymers Composed of Luminescent Ruthenium(II) Metalloligands: Importance of the Position of the Coordination Site in Metalloligands", Inorg. Chem. 2014, 53 (6), 2910-2921.

67. Watanabe, A.; Kobayashi, A.; Saitoh, E.; Nagao, Y.; Yoshida, M.; Kato, M., "Visualization of Ion Conductivity: Vapochromic Luminescence of an Ion-Conductive Ruthenium (II) Metalloligand-Based Porous Coordination Polymer", Inorg. Chem. 2015, 54 (23), 11058-11060.

68. Ashlee J. Howarth[†], Aaron W. Peters[†], Nicolaas A. Vermeulen[†], Timothy C. Wang[†], Joseph T. Hupp[†], and Omar K. Farha[*][†]"Best Practices for the Synthesis, Activation, and Characterization of Metal–Organic Frameworks",Chem. Mater., **2017**, 29 (1), pp 26–39.

69. Ying Li† [ab], Hua Xu† *[ab], Shuxin Ouyang [ab] and Jinhua Ye[abc] , "Metal–organic frameworks for photocatalysis",Phys. Chem. Chem. Phys., 2016, **18**, 7563-7572.

70. Schubert, U.; Husing, N. Synthesis of Inorganic Materials. WILEY-VCH: Germany, 2005.

71. Settle, F. A. Handbook of Instrumental Techniques for Analytical Chemistry. Prentice Hall PTR: New Jersey, 1997.

72. Cullity, B. D. Elements of X-ray Diffraction, 2nd ed. Addison-Wesley: Menlo Park, 1978. 72

73. David, W. I. F.; Shankland, K.; McCusker, L. B.; Baerlocher, Ch. Structure Determination from Powder Diffraction Data. Oxford University Press: USA, 2002.

74. Smart, L.; Moore, E. Solid State Chemistry: An Introduction. Nelson Thornes Ltd: Cheltenham, 2001.

75. http://serc.carleton.edu/research_education/geochemsheets/techniques/XRD.html

76. Bennett, D.W. Understanding Single-crystal X-ray Crystallography; Wiley-VCH: Weinheim. 2010.

77. Clegg, W. Crystal Structure Determination; Oxford University Press: Oxford; New York. 1998.

78. Fletcher, D. A.; McMeeking, R. F.; Parkin, D. J. Chem. Inf. Comp. Sci. 1996, 36, 746.

79. Settle, F. A. Handbook of Instrumental Techniques for Analytical Chemistry. Prentice Hall PTR: New Jersey, 1997. 4. Ellsworth, J. M.; zur-Loye, H. C. Dalton Trans. 2008, 5823.

80. Ellsworth, J. M.; zur-Loye, H. C. Dalton Trans. 2008, 5823.

81. Sheldrick, G.M.; SADABS, Seimens Area Detector Absorption (and other) Correction, Univ. of Gottinger, Gottinger, Germany. 1998.

82. Skoog, D. A.; Holler, F. J.; Crouch, S. R. "Principle of Instrumental Analysis". 6th ed. Thomson Brooks/Cole: Belmont, 2007.

83. Albani, J. R. "Principles and Applications of Fluorescence Spectroscopy". WileyBlackwell: New York, 2007.

84. P.A. Maggard, B. Yan, J. Luo, "Pillared Hybrid Solids with Access to Coordinatively Unsaturated Metal Sites: An Alternative Strategy", Angewandte Chemie International Edition, 44 (2005) 2553-2556.